

AD _____

Award Number: W81XWH-06-1-0449

TITLE: Early Detection of Breast Cancer via Multiplane Correlation Breast Imaging

PRINCIPAL INVESTIGATOR: Amarpreet Chawla
Ehsan Samei

CONTRACTING ORGANIZATION: Duke University
Durham, NC 27710

REPORT DATE: April 2007

TYPE OF REPORT: Annual Summary

PREPARED FOR: U.S. Army Medical Research and Materiel Command
Fort Detrick, Maryland 21702-5012

DISTRIBUTION STATEMENT: Approved for Public Release;
Distribution Unlimited

The views, opinions and/or findings contained in this report are those of the author(s) and should not be construed as an official Department of the Army position, policy or decision unless so designated by other documentation.

REPORT DOCUMENTATION PAGE				Form Approved OMB No. 0704-0188	
Public reporting burden for this collection of information is estimated to average 1 hour per response, including the time for reviewing instructions, searching existing data sources, gathering and maintaining the data needed, and completing and reviewing this collection of information. Send comments regarding this burden estimate or any other aspect of this collection of information, including suggestions for reducing this burden to Department of Defense, Washington Headquarters Services, Directorate for Information Operations and Reports (0704-0188), 1215 Jefferson Davis Highway, Suite 1204, Arlington, VA 22202-4302. Respondents should be aware that notwithstanding any other provision of law, no person shall be subject to any penalty for failing to comply with a collection of information if it does not display a currently valid OMB control number. PLEASE DO NOT RETURN YOUR FORM TO THE ABOVE ADDRESS.					
1. REPORT DATE 01-04-2007		2. REPORT TYPE Annual Summary		3. DATES COVERED 31 Mar 2006 – 30 Mar 2007	
4. TITLE AND SUBTITLE Early Detection of Breast Cancer via Multiplane Correlation Breast Imaging				5a. CONTRACT NUMBER	
				5b. GRANT NUMBER W81XWH-06-1-0449	
				5c. PROGRAM ELEMENT NUMBER	
6. AUTHOR(S) Amarpreet Chawla, Ehsan Samei Email: asc14@duke.edu				5d. PROJECT NUMBER	
				5e. TASK NUMBER	
				5f. WORK UNIT NUMBER	
7. PERFORMING ORGANIZATION NAME(S) AND ADDRESS(ES) Duke University Durham, NC 27710				8. PERFORMING ORGANIZATION REPORT NUMBER	
9. SPONSORING / MONITORING AGENCY NAME(S) AND ADDRESS(ES) U.S. Army Medical Research and Materiel Command Fort Detrick, Maryland 21702-5012				10. SPONSOR/MONITOR'S ACRONYM(S)	
				11. SPONSOR/MONITOR'S REPORT NUMBER(S)	
12. DISTRIBUTION / AVAILABILITY STATEMENT Approved for Public Release; Distribution Unlimited					
13. SUPPLEMENTARY NOTES Original contains colored plates: ALL DTIC reproductions will be in black and white.					
14. ABSTRACT One of the major deficiencies of standard mammography is the camouflaging effect of overlapping structures in the projection images that limits the rendering of breast cancer. To minimize the effect of this limiting factor, we investigated the feasibility of Multi-plane Correlation Imaging (MCI) technique. In this technique, multiple radiographic images of the breast are obtained from different angles. Angular information is used to identify and positively reinforce the lesion signals between different projections. In the first stage of this study, we investigated the optimal geometry of acquisitions in MCI which yields superior diagnostic information. Towards this end, a LG CHO mathematical observer model was constructed to assess the detectability of a simulated mass embedded in the different angular projections acquired as part of MCI. Detectability performance on various angular projections were combined using three techniques to determine a final figure of merit as a measure of the system's performance. Lastly, different components of acquisitions such as the number of angular projections and the angular span of them were changed to investigate which one of the combinations maximizes the detectability performance.					
15. SUBJECT TERMS Mammography, Tomosynthesis, Multi-projection Imaging, Laguerre-Gauss Channelized Hotelling Observer, ROC, Detectability Index, SKE, Computer Aided Detection.					
16. SECURITY CLASSIFICATION OF:			17. LIMITATION OF ABSTRACT	18. NUMBER OF PAGES	19a. NAME OF RESPONSIBLE PERSON
a. REPORT	b. ABSTRACT	c. THIS PAGE			USAMRMC
U	U	U	UU	37	19b. TELEPHONE NUMBER (include area code)

Table of Contents

	<u>Page</u>
Introduction.....	4
Body.....	5
Key Research Accomplishments.....	12
Reportable Outcomes.....	12
Conclusion.....	12
References.....	13
Appendices.....	14

INTRODUCTION

Currently, mammography is the de facto technology for breast cancer screening. Although the technology is proven to be most sensitive among other comparable screening techniques,¹ it is not without limitation. The specificity of mammography is still relatively low; only 15-30% of suspected breast lesions recommended for biopsy are actually malignant.^{2,3} At the same time the false negative rate of mammography in dense breasts can be as high as 25%.⁴

In mammography, a 3D volume of anatomical structures is collapsed into a 2D image plane. The resultant image, therefore, is a consequence of projection of overlapping anatomical structures into a complex 2D image. As a result, any abnormality in the form of breast cancer may easily get hidden behind projections of a normal tissue structures, resulting in low sensitivity. At the same time, the overlapping structures may also mimic the pathology that the radiologists are looking for, leading to high rate of false positives. An imaging technique which may alleviate the limiting factor of overlapping anatomical structures and at the same time take advantage of standard mammography imaging technique, may therefore prove to be highly effective in breast cancer screening.

In this study, we are investigating the feasibility of a new imaging technique, namely, **Multi-plane Correlation Imaging (MCI)** in which a plurality of digital radiographic images of the breast are acquired within a short interval of time from slightly different angles. These images are similar to projection images acquired in standard digital mammography, except that each of the angular projections is acquired with lower dose level than used in standard mammography. These images are then processed by a computer algorithm which utilizes spatial correlation information between different angular projections to identify and positively reinforce the lesion signals between different projections, thus minimizing the fundamental limiting factor imposed by anatomical noise on detection of lesions.

For the first stage of this study, we investigated the optimum geometry of acquisitions in MCI in terms of the number of acquisitions and the angular span of those acquisitions that yield maximum performance in a clinical detection task. A simulated mass was embedded in the multiple projections to emulate a realistic clinical task. An approach based on mathematical observer model was developed to assess the detectability of the mass. Detectability was measured in terms of Receiver Operating Characteristics (ROC). The methodology first combined cues on the detectability of mass available from multiple projections into a combined ROC as final figure of merit to measure the system's performance. Next, a specific combination of number of angular acquisitions and the angular span of these acquisitions was determined that maximized the Area under the combined ROC curve (AUC). The combination that maximizes the AUC was deemed the optimized geometry for MCI acquisitions.

BODY

Specific Aim 1: Determine the set of acquisition parameters for an MCI study. (Months 1-9)

Task 1.1: Acquire multi-projection images of 10 cadaver breast specimens with and without lesions inserted at various settings of acquisition parameters. (Months 1-3)

Progress: Work for this task is still in progress. The goal of this task was to acquire images that approximate mammographic backgrounds which could then be used for analysis in developing methodologies for the other specific aims of this study. However, due to an accelerated effort in acquiring patient data as a part of another NIH funded grant whose PI, Dr. Joseph Lo, is also co-mentor in this study, we have now acquired multi-projection images from 200 human subjects.⁵ This database was considered to be more robust and relevant to our specific aims and was therefore used for analysis in this study instead of images from cadaver specimens. Notwithstanding, we have already acquired 1 cadaver specimen. As we learn more about the administrative procedure to acquire such specimens, this process is expected to accelerate. We hope to acquire the remaining number of cadaver specimens in near future.

The first couple of months since the start of this grant were spent in securing an approval from the IRB office at Duke for retrospect use of the already acquired human subject data. The specific components of this study were determined to be in compliance with all applicable “HIPAA” regulations. Final IRB approval was received on 07/24/06.

The human subject data employed in this study were acquired about the CC or MLO orientation from 25 different but fixed angular positions by a prototype clinical multi-projection system, Siemens’ Mammomat Novation^{DR}.⁵ The database consisted of images of the left and right breasts of 82 subjects (out of 200 overall who were recruited). 492 regions-of-interest (ROIs) (2 breasts x 82 patients x 3 ROIs/projection) of size 512 x 512 each were extracted from each of these images.

Task 1.2: Develop Laguerre-Gauss Channelized Hotelling Observer incorporating the spatial correlation information available via MCI technique. (Months 1-6)

Progress: This task has been accomplished. The goal of this task was to develop an observer model which could be used to quantify the performance of MCI in detecting a simulated mass. Observers models have been used to predict human observer performance in clinically relevant visual tasks such as the detection of lesions in a complex background structure.⁶⁻⁸

As a first step to meet the objectives of this task, a lesion was inserted in the multiple angular projections acquired in MCI. The lesion was simulated in 3D. To do so, first a 2D projection profile based on a previously published model of lung nodules was generated.^{9, 10} This profile has also been applied to mammographic applications.¹¹ Starting from this profile, the surface of the central slice of the lesion was reconstructed using inverse radon transform, assuming that the lesion is isotropic and the different angular projections along the plane of the central slice would yield the same profile across the central slice. The central slice was then rotated about its

diameter to complete the simulation of a 3D lesion. Next, projections of this 3D lesion were embedded onto the different ROIs to generate 492 signal-present ROIs for each of the 25 angular projections. The ratio of the contrast of the lesion to its diameter (set to 3 mm) was determined from published contrast/lesion thickness ratios based on the acquisition kVp, target/filteration combination, compressed breast thickness, and detector type.¹² This ratio was further modified to take scattering into account. Towards that end, scatter to primary ratio were computed based on 75/25% glandular tissue/fat breast composition. The lesions were then added to the ROI in the log space such that the contrast of the lesion over the background was independent of the breast composition. Fig. 1 shows projection of the 3D lesion on the detector from three different tube angular orientations of $+21.89^\circ$, 0° , and -22.94° relative to the CC orientation. Fig. 2 shows images of ROIs with the simulated lesion embedded at the center.

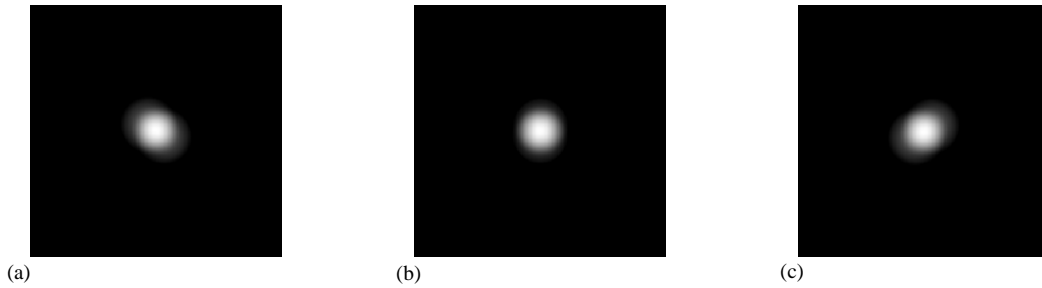


Fig. 1: Example images of projections of 3D model of a 3 mm simulated lesion. These lesions were embedded on MCI projections to emulate the lesion-present mammographic background. (a), (b), and (c) show the projections with the tube orientation at $+21.9^\circ$, 0° , and -22.9° , respectively, relative to the CC orientation.

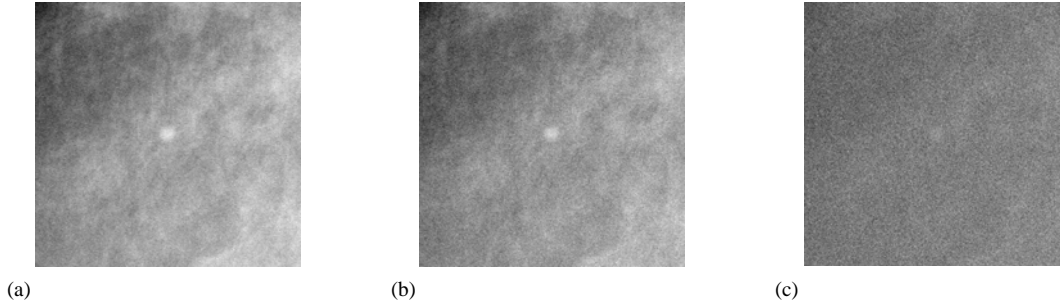


Fig. 2: Example images of ROIs with simulated lesion embedded at the center. The ROIs were extracted from full-field MCI projections, following which, projections of 3D model of a 3 mm lesion were embedded at the center of each of these ROIs.

Having inserted the masses into the different angular projections acquired in MCI, the next task was to develop an observer model that could predict the detectability of these masses over the complex mammographic backgrounds. Towards that end, a linear observer model called Channelized Hotelling Observer (CHO) was developed. The model uses functions which are a product of *Laguerre* polynomials and *Gaussians*. These functions extract essential linear features from the image thereby considerably reducing the dimensionality of the problem. Fig. 3 shows the first 9 of the 10 Laguerre-Gauss channels used in this study.

Laguerre-Gauss Channelized Hotteling Observer (LG CHO) was used to generate a set of signal-absent and signal-present decision variables for ROIs from each angular projection. Non-parametric ROC curves were then derived by simple thresholding on the probability density function (*pdf*) of the decision variables. While testing using the LG CHO, signal in each of the ROIs was analyzed with the signal-known exactly (SKE) methodology, assuming that the lesion embedded on different ROIs within the same angular projection have approximately the same shape. ROC for each of the 25 angular projections was obtained (Fig. 4). The area under the mean ROC curve (AUC) was subsequently determined using the trapezoidal rule.

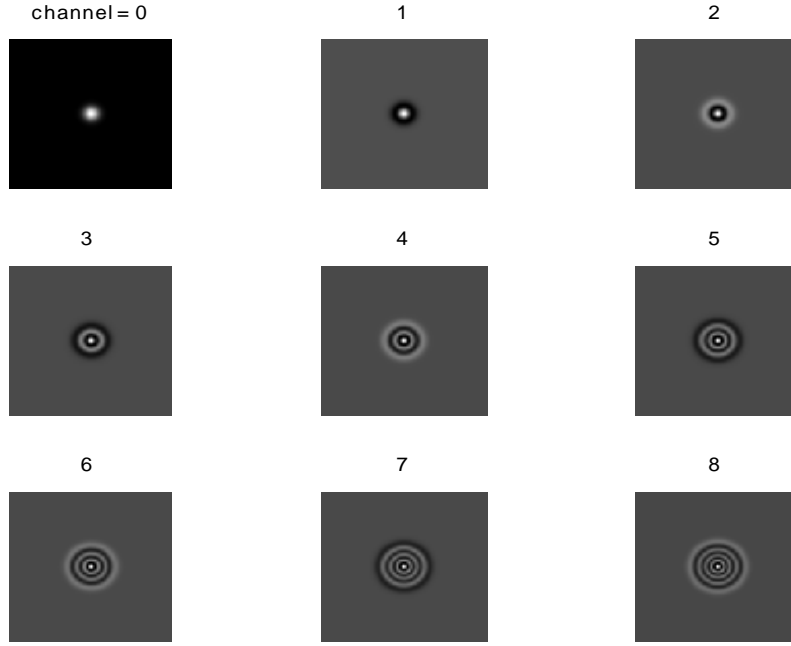


Fig. 3: First 9 of the 10 Laguerre-Gauss channels used in to develop the observer model for task 1.2.

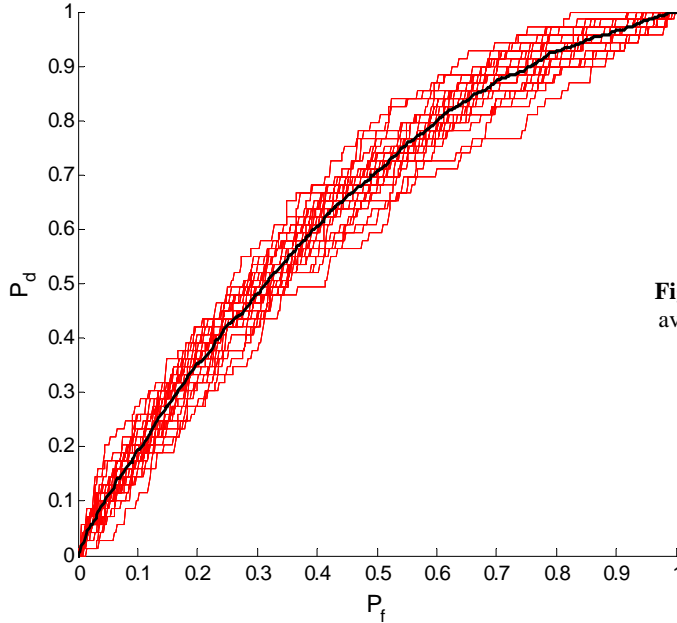


Fig. 4: ROCs of 25 projections and the average of those with the final AUC = 0.6417

Finally, 25 ROCs obtained from the 25 angular projections were fused into one final index of performance to indicate the overall system's performance in its ability to detect the embedded mass. Towards that end, three methods were used. For the first method, the 25 ROCs were simply averaged along the true positive fractions to yield the combined ROC associated with the detection of lesion in all the projections. In the second method, the signal-present and signal-absent test statistics from different projections were averaged to determine the final test statistics. These values were then used to determine the combined ROC.

For the third ROC fusion method, a modification of a recently published Bayesian decision fusion algorithm was used.¹² In this case, first ROC for each angular projection in the training dataset was determined. The training dataset comprised of 429 ROIs for each angular projection. Next, for each of the 69 ROIs in the testing dataset, signal-present decision variable was calculated by determining the response of the image embedded with i^{th} lesion to i^{th} lesion template and the corresponding signal-absent response by determining the response of the image itself (without the lesion embedded) to the i^{th} lesion template. Binary observer decision, β_i , to the i^{th} image was computed as

$$\begin{aligned}\beta_i &= \text{step}(\lambda_1^i - \lambda_0^i) \\ &= \begin{cases} 1 & \text{if } \lambda_1^i \geq \lambda_0^i \\ 0 & \text{if } \lambda_1^i < \lambda_0^i, \end{cases}\end{aligned}\quad (1)$$

i.e., the binary decision for an i^{th} image was 1 if the signal-present decision variable, λ_1^i , exceeded signal-absent decision variable, λ_0^i , but 0 otherwise. From the above equations it is clear that the threshold for correct observer outcome of an i^{th} image is λ_0^i . The corresponding values of probability of true positive, P_d , and of false positives, P_f , were determined from the ROCs of the 25 angular projections in the training dataset. Assuming that the binary decisions were statistically independent, the PDFs of the fused decision variables for signal-present and null hypothesis were then obtained as

$$\begin{aligned}P(\lambda_{fusion} | H_1) &= \prod_{\theta=1}^{25} (p_d^\theta)^{\beta_i} (1 - p_d^\theta)^{1-\beta_i} \\ P(\lambda_{fusion} | H_0) &= \prod_{\theta=1}^{25} (p_f^\theta)^{\beta_i} (1 - p_f^\theta)^{1-\beta_i},\end{aligned}\quad (2)$$

where, θ is an index for angular projection. Having found the signal-present and signal-absent decision variables, the probability density functions of each were computed and ROC determined.

ROC curves and the corresponding AUCs obtained from the three techniques are shown in Fig. 5. While AUC obtained from a single CC projection was 0.652, AUC obtained from an average of ROCs obtained from 25 projections was 0.642. Simple averaging of test statistics yielded an AUC of 0.815. An AUC of 0.946 was obtained from the Bayesian decision fusion technique.

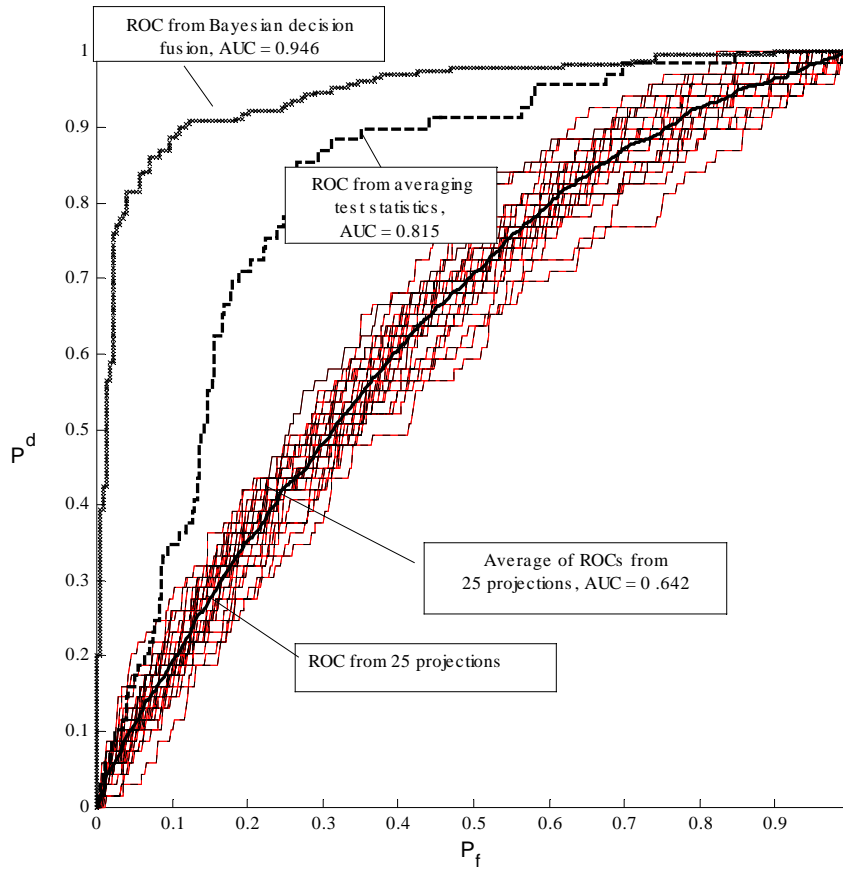


Fig. 5: ROCs of 25 projections and the average of those with the final AUC = 0.6417. Also shown are the ROCs obtained from the three other fusion techniques. The angular span of the projections was 44.8°.

The work on this task was started well in advance in anticipation of its application in two of the remaining aims. It resulted in the following publication in the proceedings of SPIE's conference on Medical Imaging in 2006:

A. S. Chawla, R. Saunders, C. Abbey, D. DeLong and E. Samei, "Analyzing the effect of dose reduction on the detection of mammographic lesions using mathematical observer models," Proc. SPIE 6146, 61460I-61461 - 61460I-61412 (2006).

Task 1.3: Apply the observer model on the image dataset to determine the optimum set of acquisition parameters, namely, maximum number of oblique views required, the specific angulations at which they should be acquired and the optimum dose level at which each of those should be acquired. (Months 7-9)

Progress: This task has been accomplished. The ROC fusion methodologies were applied to evaluate the effect of changing original acquisition parameters of MCI. This was evaluated at 25 different dose levels whose magnitudes were less than that used for actual clinical acquisitions.

These reduced dose levels were simulated by adding radiographic noise to each of the ROIs to create images with a noise appearance similar to that caused by reduction in clinical radiation dose. Noise equivalent of a particular dose level was determined using a novel algorithm, which has been reported earlier in detail.¹³ The two acquisition parameters evaluated were the angular range of projections and the number of angular projections within each angular range.

Fig. 6 shows variation of AUC for different number of angular projections spanning a total angular arc in the 3.6-44.8° range using the Bayesian decision fusion technique. The dose level of each acquisition is equal to $1/25^{th}$ of standard mammographic screening dose level leading to increased dose level with increasing number of angular projections considered. At each angular range, the AUC increases with the increase in number of angular projections indicating the potential improvement in detection due to the MCI technique. The change in AUC at each angular range is, however, minimal after approximately 10 projections. Noteworthy, is the fact that an angular span of 11.4° yields the highest AUC when fusing only two projections.

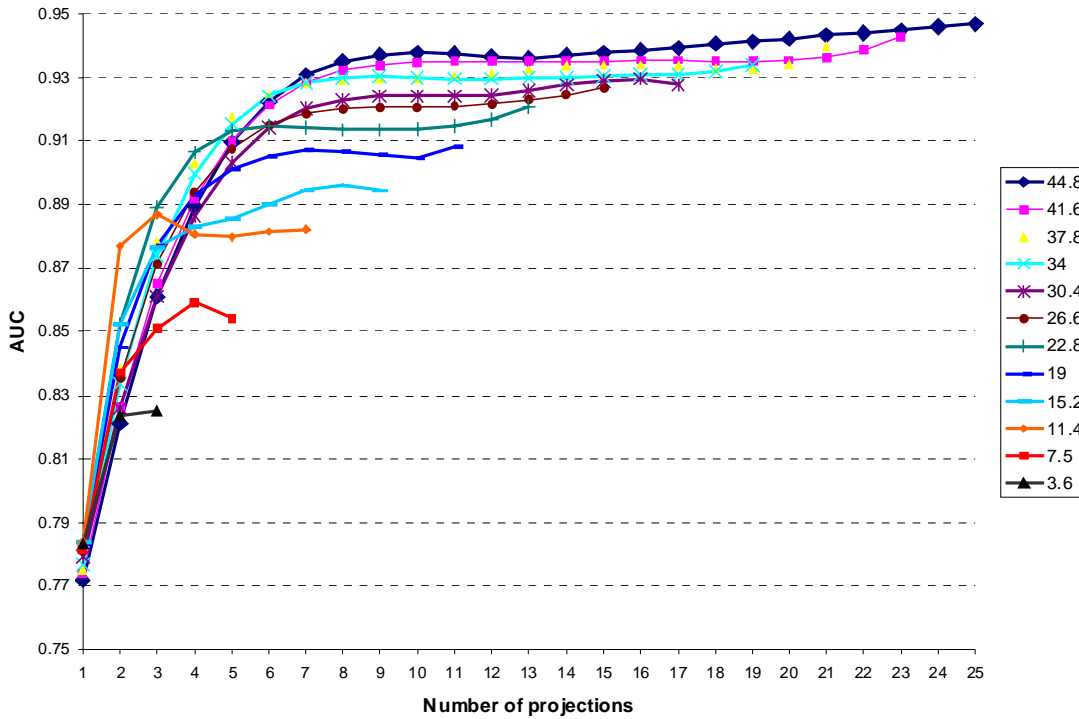


Fig. 6: Variation of AUC for different number of angular projections spanning a total angular arc in the 3.6-44.8° range using the Bayesian decision fusion technique. The dose level of each acquisition is equal to $1/25^{th}$ of standard mammographic screening dose-level leading to increased dose level with increasing number of angular projections considered to reach a maximum of conventional dual-view screening dose at 25 projections.

A second dose configuration was evaluated in which the total dose level is linearly divided among the different projections and hence the total dose delivered to the patient does not increase with an increase in the number of projections considered for decision fusion. Fig. 7 shows variation of AUC under these conditions using the Bayesian decision fusion technique. In this case, for all angular spans, the AUC first increases and then decreases as the number of projections is increased.

Both the dose configurations show that the highest AUC is obtained by combining information from just two projections with an angular span of 11.4° .

To summarize our findings, we found that the detectability of lesion in MCI is dependent on the number of projections used, the total angular span of those projections and their acquisition dose level. An optimization technique to quantify the effects of changing acquisition parameters was established. It was found that if the total dose level is held constant at $1/25^{th}$ of the standard dual-view mammographic screening dose, the highest detectability performance is observed when considering only two projections spread along an angular arc of span 11.4° . Future work will confirm this optimization at higher dose levels. The methodology presented here for optimizing acquisition parameter are generic in nature and, therefore, can be easily adopted for optimizing the acquisition parameters for other breast imaging methods, such as Digital Breast Tomosynthesis, where the final figure of merit is contingent on decisions made on a plurality of image slices.

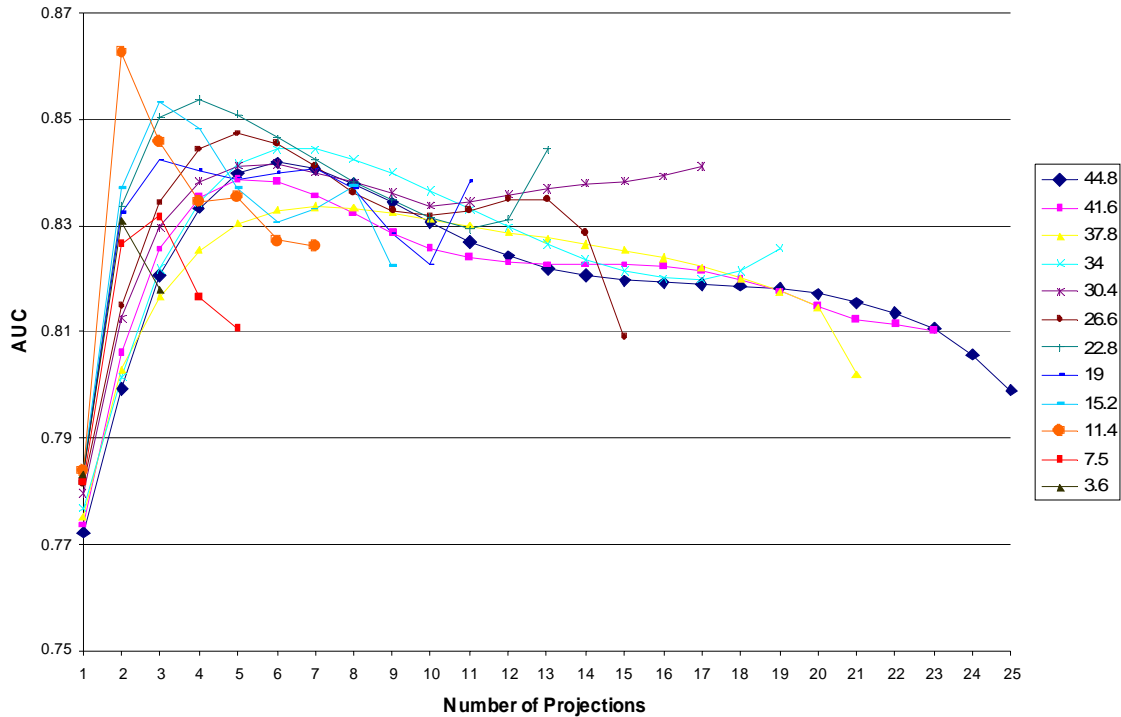


Fig. 7: Variation of AUC under iso-study dose conditions using the Bayesian decision fusion technique. The total dose level, equal to $1/25^{th}$ of standard dual-view mammographic screening dose level, is linearly divided amongst the different projections and hence the total dose delivered remains constant at this dose level.

Work for this specific task resulted in the following publication in the proceedings of SPIE's conference on Medical Imaging in 2007:

A. S. Chawla, E. Samei, and C. Abbey, "A mathematical model approach toward combining information from multiple image projections of the same patient," Proc. SPIE 65101,K1-11, (2007)

Specific Aim 2: Extend single-view CAD processing methods used for conventional mammography for MCI implementation using a multi-plane correlation rule. (Months 10-21)

Progress: We have initiated the task of extending an existing single-view and a recently published dual-view CAD algorithm for the purpose of MCI.¹⁴ Since the work is in its preliminary stage, we will defer a report on this task to a subsequent annual summary.

KEY RESEARCH ACCOMPLISHMENTS

- An observer model approach was developed to quantify the effect of changing acquisition parameters on diagnostic image quality of radiographic images.
- Multi-plane correlation imaging (MCI) was demonstrated to improve sensitivity over standard mammography.
- Optimum geometry of MCI acquisitions that maximizes image quality in terms of detectability of a simulated mass was investigated.
- The methodologies developed in this phase of the project will be key to meeting the goals of the remaining specific aims of this study.

REPORTABLE OUTCOMES

The following manuscripts are attached as appendices 1 and 2 with the same numbers. The names of the fellow (**Chawla**) and mentor (**Samei**) are boldfaced for emphasis.

1. A. S. **Chawla**, R. Saunders, C. Abbey, D. DeLong and E. **Samei**, "Analyzing the effect of dose reduction on the detection of mammographic lesions using mathematical observer models," Proc. SPIE 6146, 61460I-61461 - 61460I-61412 (2006).
2. A. S. **Chawla**, E. **Samei**, and C. Abbey, "A mathematical model approach toward combining information from multiple image projections of the same patient," Proc. SPIE 65101,K1-11, (2007)

CONCLUSIONS

We have demonstrated feasibility of Multi-plane correlation imaging (MCI) as a technique for breast cancer screening. Detectability of a simulated mass increased with increase in the number of angular projections, even as the total dose delivered to the patient remained constant. The technique demonstrated superior diagnostic performance when considering only two projections spread along an angular arc of span 11.4° . Future work with cadaver specimens will substantiate the results of the present findings.

REFERENCES

- ¹ L. Tabar and P. B. Dean, "The Control of Breast Cancer through Mammography Screening," *Radiologic Clinics of North America* **25**, 993-1005 (1987).
- ² D. B. Kopans, "The positive predictive value of mammography," *American Journal of Roentgenology* **158**, 521-526 (1991).
- ³ D. D. Adler and M. A. Helvie, "Mammographic biopsy recommendations," *Current Opinion in Radiology* **4**, 123-129 (1992).
- ⁴ R. E. Bird, T. W. Wallace and B. C. Yankaskas, "Analysis of cancers missed at screening mammography," *Radiology* **184**, 613-617 (1992).
- ⁵ S. Singh, G. D. Tourassi and J. Y. Lo, "Breast mass detection in tomosynthesis projection images using information-theoretic similarity measures," *Proc. SPIE* **6514**, 651415 (2007).
- ⁶ M. P. Eckstein, C. K. Abbey and E. O. Bochud, "The effect of image compression in model and human performance," *Proc. SPIE* **3663**, 243-252 (1999).
- ⁷ M. P. Eckstein, C. K. Abbey and J. S. Whiting, "Human vs. model observers in anatomic backgrounds," *Proc. SPIE* **3340**, 16-26 (1998).
- ⁸ A. E. Burgess, F. L. Jacobson and P. F. Judy, "Human observer detection experiments with mammograms and power-law noise," *Med. Phys.* **28**, 419-437 (April 2001).
- ⁹ R. S. Saunders, E. Samei and C. Hoeschen, "Impact of resolution and noise characteristics of digital radiographic detectors on the detectability of lung nodules," *Med. Phys.* **31**, 1603-1613 (2004).
- ¹⁰ E. Samei, M. Flynn and W. Eyler, "Simulation of subtle lung nodules in projection chest radiography," *Radiology* **202**, 117-224 (1997).
- ¹¹ A. E. Burgess, F. L. Jacobson and P. F. Judy, "Human observer detection experiments with mammograms and power-law noise," *Med. Phys.* **28**, (2001).
- ¹² J. L. Jesneck, L. W. Nolte, J. A. Baker, C. E. Floyd and J. Y. Lo, "Optimized approach to decision fusion of heterogeneous data for breast cancer diagnosis," *Med. Phys.* **33**, (2006).
- ¹³ R. S. Saunders and E. Samei, "A method for modifying the image quality parameters of digital radiographic images," *Med. Phys.* **30**, 3006-3017 (2003).
- ¹⁴ R. S. Saunders, E. Samei, N. Majdi-Nasab and J. Y. Lo, "Initial human subject results for breast bi-plane correlation imaging technique," *Proc. SPIE* **6514**, **651423**, 1-7 (2007).

APPENDIX

1. A. S. **Chawla**, R. Saunders, C. Abbey, D. DeLong and E. **Samei**, "Analyzing the effect of dose reduction on the detection of mammographic lesions using mathematical observer models," Proc. SPIE 6146, 61460I-61461 - 61460I-61412 (2006). 15
2. A. S. **Chawla**, E. **Samei**, and C. Abbey, "A mathematical model approach toward combining information from multiple image projections of the same patient," Proc. SPIE 65101, K1-11, (2007)..... 27

Analyzing the effect of dose reduction on the detection of mammographic lesions using mathematical observer models

Amarpreet S. Chawla¹, Robert Saunders², Craig Abbey³, David DeLong⁴, Ehsan Samei²

¹Departments of Radiology and of Biomedical Engineering, Duke University

²Departments of Radiology, Physics and of Biomedical Engineering, Duke University

³Department of Biomedical Engineering, University of California, Davis

⁴Department of Biostatistics and Bioinformatics, Duke University

ABSTRACT

The purpose of this study was to determine the effect of dose reduction on the detectability of breast lesions in mammograms. Mammograms with dose levels corresponding to 50% and 25% of the original clinically-relevant exposure levels were simulated. Detection of masses and microcalcifications embedded in these mammograms was analyzed by four mathematical observer models, namely, the Hotelling Observer, Non-prewhitening Matched Filter with Eye Filter (NPWE), and Laguerre-Gauss and Gabor Channelized Hotelling Observers. Performance was measured in terms of ROC curves and Area under ROC Curves (AUC) under Signal Known Exactly but Variable Tasks (SKEV) paradigm. Gabor Channelized Hotelling Observer predicted deterioration in detectability of benign masses. The other algorithmic observers, however, did not indicate statistically significant differences in the detectability of masses and microcalcifications with reduction in dose. Detection of microcalcifications was affected more than the detection of masses. Overall, the results indicate that there is a potential for reduction of radiation dose level in mammographic screening procedures without severely compromising the detectability of lesions.

Keywords: Dose, Simulation, Mammography, Non-prewhitening Matched filter with Eye filter, Laguerre-Gauss, Gabor, Hotelling Observer, AUC, ROC, SKEV.

INTRODUCTION

Early detection of breast cancer is largely contingent on the image quality of mammograms. There are many aspects of image quality. Among factors like the physical properties of the detector, the beam quality and others, the image quality of mammograms also depends on the amount of x-ray exposure to the detector and hence the amount of dose delivered to the patient. However, there is no strict protocol for the dose level. The recommendations of the National Council on Radiation Protection and Measurements (NCRP) are for the mean glandular doses (MGD) to be lower than 2 mGy for images acquired with anti-scattering grids and lower than 4 mGy without anti-scattering grids (1). A survey of patients undergoing mammography found MGD in the 0.3–12 mGy range (2).

An increase in dose delivered to the breast improves image quality parameters like sharpness, noise and contrast. At the same time, the dose level has to be kept below a certain threshold to minimize radio-toxicity of mammographic screening exams. This is particularly important since approximately 99.5% of the screened population are retrospectively found to have no breast cancer, and only 15–30% of suspected breast lesions recommended for biopsy are actually malignant (3, 4). A recent report by National Academy of Sciences (NAS) (5) concludes that there are evidences that even the smallest dose of low-level ionizing radiation causes increased health risks to humans. It is therefore important that to minimize these risks, the patient dose in x-ray mammography be kept as low as possible while also ensuring that the image quality required for a given detection task is not compromised.

An important factor why dose can be potentially reduced in mammography is the fact that detectability of lesions is often confounded by overlapping anatomical structures – a characteristic inherent to any projection imaging technique. This limitation of mammograms in rendering masses and microcalcifications hidden in dense fibroglandular tissue is not governed by the amount of x-ray exposure and hence the dose level delivered to the breast. In fact it has been suggested that anatomical noise could be the biggest factor limiting the detection of breast cancer, both by radiologists and by computer assisted diagnosis (CAD) systems (6, 7). This indicates that the dose in mammography could be lowered without profound effect on the detectability of lesions.

Research on optimizing the benefit to radiation risk ratio of digital mammographic screening procedures is active (8). Berns (9) et al. showed that dose values could be lower for digital systems than those for screen-film systems. A recent study by Gennaro et al. (10) on breast phantoms concluded that this dose reduction factor could be as much as 50% while still preserving image quality above screen/film standards.

In this work, the impact of reduced dose on the detection of breast lesions was studied using mathematical observer models. The detectability of simulated masses and microcalcifications at reduced dose levels was analyzed and compared with the performance on mammograms acquired with clinical dose levels. To quantify the detectability performance, four mathematical observers were implemented. The results were characterized in terms of ROC and the area under the ROC curve (AUC) to compare detectability at different dose levels.

MATERIALS AND METHODS

The study was conducted in multiple steps. First, breast lesions were simulated and embedded on normal mammographic backgrounds acquired at clinical dose levels. Secondly, simulated dose-equivalent noise were added onto these images to emulate images acquired at lower dose levels. Next, four mathematical observer models were implemented. These were the Non Pre-whitening observer with Eye filter (NPWE), Hotelling observer and two Channelized Hotelling Observer (CHO), namely Gabor and Laguerre-Gauss channelized Hotelling observers. Image quality was measured in terms of Signal-to-Noise Ratio (SNR) in the case of NPWE and Hotelling Observers, and Receiver Operating Characteristic (ROC) curves and Area-Under-ROC Curve (AUC) in the case of CHOs. To simulate real-clinic like situations, a signal-known-exactly-but-variable (SKEV) paradigm was used and the background was known statistically. Finally, an analysis was performed to test the statistical significance of differences observed in AUCs obtained at the different dose-levels. The following describe these steps in detail.

A. Image Database

Mammographic images used in this study were clinically-acquired at 25-30 kVp range with molybdenum anode using a clinical flat-panel cesium iodide-based digital mammography system (Senographe 2000D, GE Medical Systems, Milwaukee, WI). A total of 300 normal craniocaudal view mammograms were used. This included the signal (lesion)-absent set of backgrounds which were used for training the observer models. Another set of signal-present images were generated by digitally inserting realistic simulated masses and microcalcifications in signal-absent backgrounds by a routine previously published (11, 12). This routine relied on the measured characteristics of real lesions to create simulated lesions with a realistic appearance. Two types of breast masses, namely benign and malignant, and two types of microcalcifications, namely pleomorphic and fine linear branching, were simulated

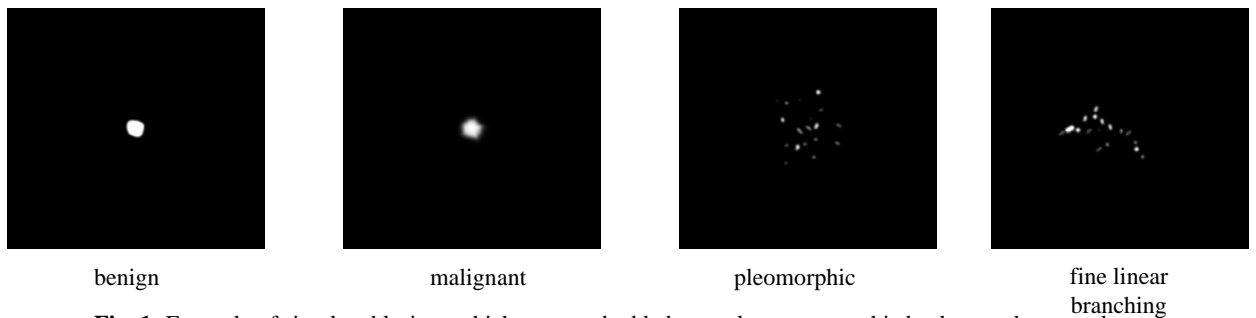


Fig. 1: Example of simulated lesions which were embedded on real mammographic backgrounds to emulate the signal-present hypothesis. Images in the left column show benign and malignant masses. Images in the right column show fine linear branching and pleomorphic malignant microcalcifications.

with sizes in the 4-8 mm range. Fifty different realizations were formed for each lesion. Fig. 1 shows the three types of lesions simulated. Following the insertion of the lesions, a noise modification routine was used to add radiographic noise to clinically-acquired mammograms to create images with a noise appearance similar to that caused by a reduction in radiation dose. Noise equivalent of a particular dose level was determined using a novel algorithm, which has been reported earlier in detail (13). The routine accounted for the quantum noise variance, the detector transfer properties, the scattered radiation and for the impact of attenuation due to breast structures on noise. By changing the noise magnitude, dose reduction corresponding to half (50%) and quarter (25%) of the original clinical exposure levels were simulated. Image post-processing techniques typical of clinical mammograms were applied to the images. To determine the appropriate window and level parameters for each mammogram, an experienced mammographer windowed and leveled each image individually. The resultant images looked identical to those that are viewed by radiologists in the clinic. Fig. 2(a) shows an ROI of a typical mammogram with a malignant mass located at the center of the image. Figs 2(b) & 2(c) show the same mammogram with added simulated noise corresponding to half and quarter the full-dose level respectively. At each dose-level, breast lesions were placed at the center of 50 mammographic backgrounds creating a total of 50 signal-present images for each type of lesion. To simulate real clinical situations, the backgrounds corresponding to these 50 signal-present images were different from the backgrounds without signal. Thus out of 300 mammographic backgrounds available in the database only 250 normal mammograms were used to test the signal-absent hypothesis.

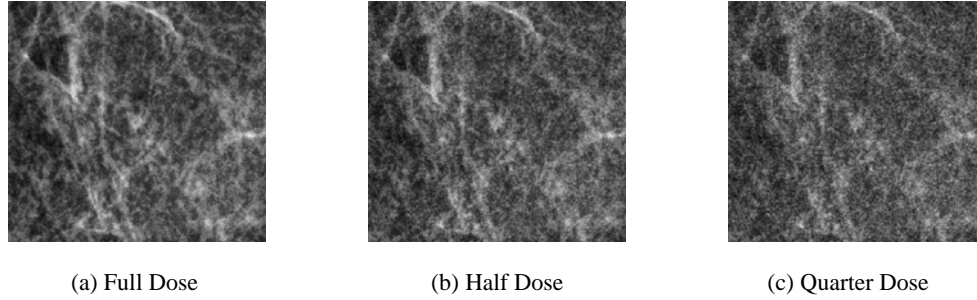


Fig. 2: Example ROIs of signal-present mammograms with a malignant lesion present at the center of it. (a) shows an ROI of a mammogram acquired with clinical dose level. (b) and (c) show the same ROI with noise corresponding to half and quarter of the full-dose level respectively added to the ROI in (a)

B. Algorithmic Observer Models

Algorithmic observer models have been used to predict human observer performance in clinically relevant visual tasks such as the detection of lesions in a complex background structure. It has been shown earlier that linear observers models like non-prewhitening matched filter, Hotelling and Gabor channelized Hotelling observers are good predictors of human visual performance under various tasks over real anatomic backgrounds (14-17). In this section a brief overview of various observer models used in this work will be presented.

i) Hotelling SNR:

If the anatomical background is assumed to be statistically stationary and the system is linear-shift invariant, it is possible to determine Hotelling Observer SNR in the Fourier domain. Since the Hotelling observer is a pre-whitening linear observer, its SNR can be calculated as (18, 19):

$$SNR_{Hot}^2 = 2\pi \int_0^{f_N} \frac{|S(f)|^2 |H(f)|^2}{W(f)} f df, \quad (1)$$

where, f is the radial frequency, f_N is the Nyquist frequency of the detector, $H(f)$ is the modulation transfer function of the system, $S(f)$ is the Fourier transform of the contrast profile of the nodule to be detected and $W(f)$ is the noise power spectrum of a mammogram with the nodule present.

ii) Nonprewhitening Matched Filter with Eye (NPWE) SNR

Nonprewhitening matched filter (NPW) is a simple template-matching observer which uses expected signal as a cross-correlation template. NPW differs from Hotelling observer in that it does not compensate for statistical variation in the background and hence cannot be used on statistically non-stationary backgrounds. The model reduces to the ideal observer for SKE/BKE tasks in white noise (16). NPW can be extended to incorporate the effect of human vision in detection tasks. This is done by filtering the template with the contrast sensitivity function of the human visual system. This model is called NPWE, where the added “E” stands for “eye filter”. The SNR of NPWE can then be determined, just like Hotelling SNR under similar assumptions of the stationarity of the noise and linear-shift invariance of the system. The SNR is given by,

$$SNR_{NPWE}^2 = 2\pi \frac{\left(\int_0^{f_N} |S(f)|^2 V(f)^2 |H(f)|^2 f df \right)^2}{\int_0^{f_N} S(f)^2 V(f)^4 |H(f)|^2 W(f) f df}, \quad (2)$$

where $V(f)$ is the transfer function of visual-response and the other variables are as defined earlier. $V(f)$ is approximated as:

$$V(f) = f^{1.5} \exp(-cf^{0.68}), \quad (3)$$

where c is a scale factor to yield maximum visual response at 4 cycles/deg, f is linear frequency in cycles/mm. Consequently for a normal viewing distance of 50 cm, $c = 3.21585 \text{ mm}^2$. Note that the visual response affects both the signal and the noise on the image as perceived by the observer.

Channelized Hotelling Observer (CHO)

Hotelling Observer is a linear observer. It uses a linear function of the pixels of an image and takes correlation in the image background into account to compute its test statistics. Since Hotelling observer takes into account knowledge of randomness in the background, it is a pre-whitening matched filter, however, with an important distinction that it is applicable on non-stationary backgrounds. In a SKE/BKE case, Hotelling observer would reduce to ideal linear observer. Hotelling observer requires an estimate of the sample variance-covariance matrix from the original images to incorporate statistical fluctuations in the image. To estimate the variance-covariance matrix from the limited number of mammograms clinically available, it is necessary to reduce the size of the sample covariance matrix. To this end, functions called linear feature could be used to extract essential features from the image. Much like in Principal Component Analysis, images are represented as weighted sum of few smooth orthonormal functions centered at the signal location thereby considerably reducing the dimensions of the covariance matrix. In this study, two such functions, namely the Laguerre-Gauss and Gabor Functions were used to reduce the problem of dimensionality. In this section, first the concept of channelized linear observer will be revisited followed by a description of the two functions and their implementation. The readers are referred to some of the excellent references on this subject for further details (14, 16, 18, 20, 21).

A linear observer computes decision variables by computing correlation between the signal template and the images. Towards this end, first responses of the images to each of the transformation channel are computed. The channel responses are calculated as the dot-product between the channels vector and the signal (lesion)-present image vector, signal (lesion)-absent image vector (also referred to as background vector) and signal (lesion)-only

image vector. Response to i^{th} lesion has been denoted here as R_s^i . R_{gI}^i is the response of an i^{th} mammographic background with i^{th} lesion embedded in it, i.e. the i^{th} signal-present image. R_{g0}^j is the response of j^{th} signal-absent background. The signal template or the channel weights corresponding to each i^{th} lesion is determined as

$$w_c^i = (K_c)^{-1} R_s^i \quad (4)$$

where K_c is the covariance matrix of the mammograms. The above equation gives Hotelling observer its prewhitening properties. The covariance matrix was determined from signal absent images since the inserted lesions were of low contrast and did not affect the covariance matrix.

Finally, the decision variables for signal-present hypothesis and null hypothesis were computed as the dot-product of signal-template and channel response of the signal-present and signal-absent mammograms, respectively. For each i^{th} signal-present image, decision variable corresponding to signal-present hypothesis was computed as dot-product of that image with the i^{th} lesion template, whereas decision variables for signal-absent hypothesis were calculated as dot-products of signal-absent backgrounds with the i^{th} lesion template. Thus for each i^{th} lesion, a single decision variable corresponding to signal-present hypothesis was computed, whereas 250 decision variables were computed for the 250 signal-absent backgrounds available in the database. This was repeated for all the 50 lesion templates available in the databases. These decision variables, also called likelihood ratios or the expected response of the model to images, are given by

$$\begin{aligned} \lambda_1^i &= (w_c^i)^t R_{gI}^i \text{ for } i^{th} \text{ lesion present image,} \\ \lambda_0^{ij} &= (w_c^i)^t R_{g0}^j \text{ for } j^{th} \text{ lesion-absent background,} \end{aligned} \quad (5)$$

where i varies between 1 and 50, and j varies from 1 to 250. This methodology is in line with the SKEV paradigm in which each of the 50 signal-present image had a different but known lesion present. 50 ROC curves were, therefore, obtained for each of the 50 lesions using this procedure. These curves were non-parametric in nature and were derived by simple thresholding on the probability density function (*pdf*) of the decision variables. These 50 ROC curves were then averaged along their true-positive fractions to generate a final ROC. Area Under Curve (AUC) to analyze the performance of the model was determined using the trapezoidal rule.

iii) Laguerre-Gauss Channelized Hotelling Observer

LG CHO is a linear observer model which is similar to a Hotelling observer but is computationally simpler. The Laguerre-Gauss channels are smooth function which are a product of *Laguerre* polynomials and *Gaussians*. The functions use a distance scale related to the signal radius. This value which defines the variance of the *Gaussian*, is iteratively adjusted to maximize the area under the ROC curves. A value of 8 was found to maximize AUC in the present study. A total of 10-channels were used (generally 6 channels are sufficient for characterizing isotropic signals (20)). As shown in Fig. 1, the signals (simulated lesions) used in our study were isotropic within certain degrees of approximation, although clustered microcalcifications did not fall into this category.

iv) Gabor Channels:

Although Laguerre-Gauss channels are easy to implement, they do not mimic the contrast sensitivity of the

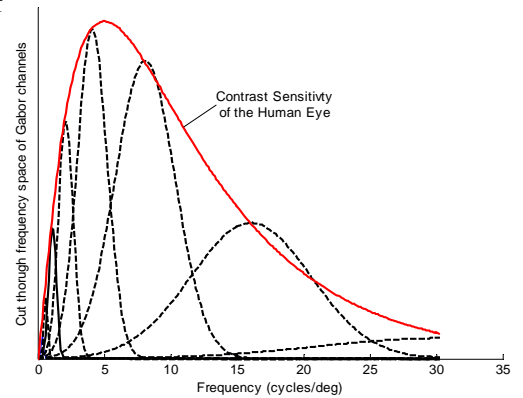


Fig. 3: Comparison of frequency response of Gabor channels with contrast sensitivity of the human eye. Octave Bandwidth of Gabor channels was 1, centered at frequencies [0.5,1,2,4,16,32] cpd, each oriented at 0°.

human eye. Fig. 3 shows this behavior of Gabor channels. It is clear from the figure that Gabor channels sample the contrast sensitivity of human eye in the frequency domain. The figure also illustrates the band-pass characteristics of the Gabor channels. An octave bandwidth of 1 was used in this study. Psychophysical studies in the past have confirmed that an octave bandwidth of 1 is a reasonably good estimate of human visual system when it is tuned to a particular frequency (22). Central frequencies chosen were 0.5, 1, 2, 4, 8, 16, 32 cycles/degree with orientations at 0° , 45° , 90° , and 135° . These with the odd and even phases add to a total of 56 channels.

C. Evaluation of Statistical Significance

An analysis was conducted to test the statistical significance of differences in AUCs obtained for detection at different dose levels. This was performed as follows: at each dose-level, 500 bootstrap samples of signal-present images were paired with 500 bootstrap samples of backgrounds. For example, the first set of 50 signal-present images obtained from the first of 500 bootstrap samples of signal-present images was paired with the first set of 250 signal-absent backgrounds obtained from the first of 500 bootstrap samples of the backgrounds. For this set of 50 signal-present and 250 signal-absent images, one ROC curve was determined by the method described in subsection (iii). This procedure was repeated for all the paired (k, k) , $k \in 1 \dots 500$, numbered bootstrap sample obtaining a set of 500 ROCs. From each of these curves, an AUC was computed. Thus a set of 500 AUCs was obtained for each dose-level. The AUCs were then subtracted in pair and the mean of differences and the standard deviation of the differences were computed as an approximation to the standard error of the difference of the means of the AUCs. If the ratio of the mean of differences and the standard error of differences was more than 2, the differences seen in AUCs at different dose levels were noted as being statistically significant.

RESULTS

Fig. 4 shows the Hotelling observer and NPWE SNRs. Values of Hotelling observer SNR (\pm std) for benign and malignant masses at the three dose levels were in the 14.30–10.15 (\pm 4.5–2.9) and 5.21–5.08 (\pm 1.60–1.53) ranges, respectively. For fine linear branching and pleomorphic microcalcifications, these values were in the 25.13–17.11 (\pm 8.5–5.7) and 25.97–5.08 (\pm 15.6–10.6) ranges, respectively.

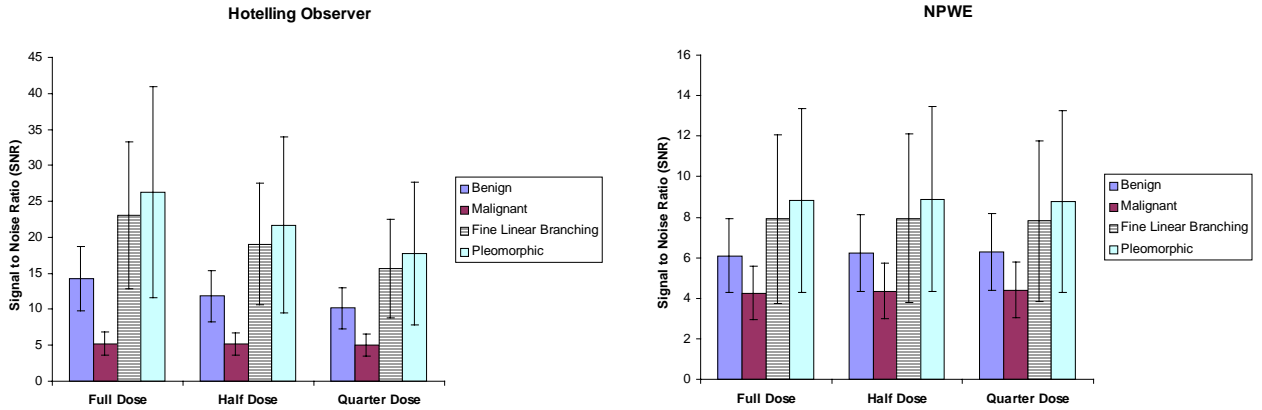


Fig. 4: Illustration of computed SNRs computed with NPWE and Hotelling observers. The standard deviation in the measurement of SNRs are also plotted. Full-dose denotes the clinical dose level used in standard mammographic screening.

Fig. 5 and Fig. 6 show ROC curves obtained from Gabor and Laguerre-Gauss channelized Hotelling observers (CHOs), respectively. For each type of breast lesion under consideration ROC curves obtained from LG CHO under different dose level conditions overlap. ROC curves obtained from Gabor CHO for the detection of malignant masses and microcalcifications under the three dose level conditions also overlap. For the detection of benign masses with Gabor CHO, however, ROC curve for the full-dose level is higher at the low false-positive portion of the ROC curves compared to those obtained at 50% or 25% of the full dose level. Similar trends are observed in the values for Area Under ROC Curves (AUC). These values with their associated standard errors are plotted in Fig. 7.

The AUC (\pm std) for the three dose levels obtained from Gabor CHO for benign and malignant masses are in the 0.975–0.996 (\pm 0.005) and 0.997–0.998 (\pm 0.001) ranges, respectively. For fine linear branching and pleomorphic microcalcifications, these values are in the 0.673–0.741 (\pm 0.02) and 0.721–0.761 (\pm 0.02) ranges, respectively. The AUC (\pm std) obtained from Laguerre-Gauss CHO for benign and malignant masses are in the 0.988–0.996 (\pm 0.003) and 0.990–0.994 (\pm 0.002) range respectively. For fine linear branching and pleomorphic microcalcifications these values are in the 0.817–0.840 (\pm 0.02) and 0.723–0.784 (\pm 0.02) range respectively. The mean of differences (\pm standard error) in AUCs obtained at the three dose levels are plotted in Fig. 8. Except in the case of detection of benign lesions with Gabor CHO, a paired t-test evaluation on detectability of lesions at different dose levels with the two CHOs showed that the differences in AUCs, as the dose is reduced to 50% or 25 %, were not statistically significant (the t-values were < 2).

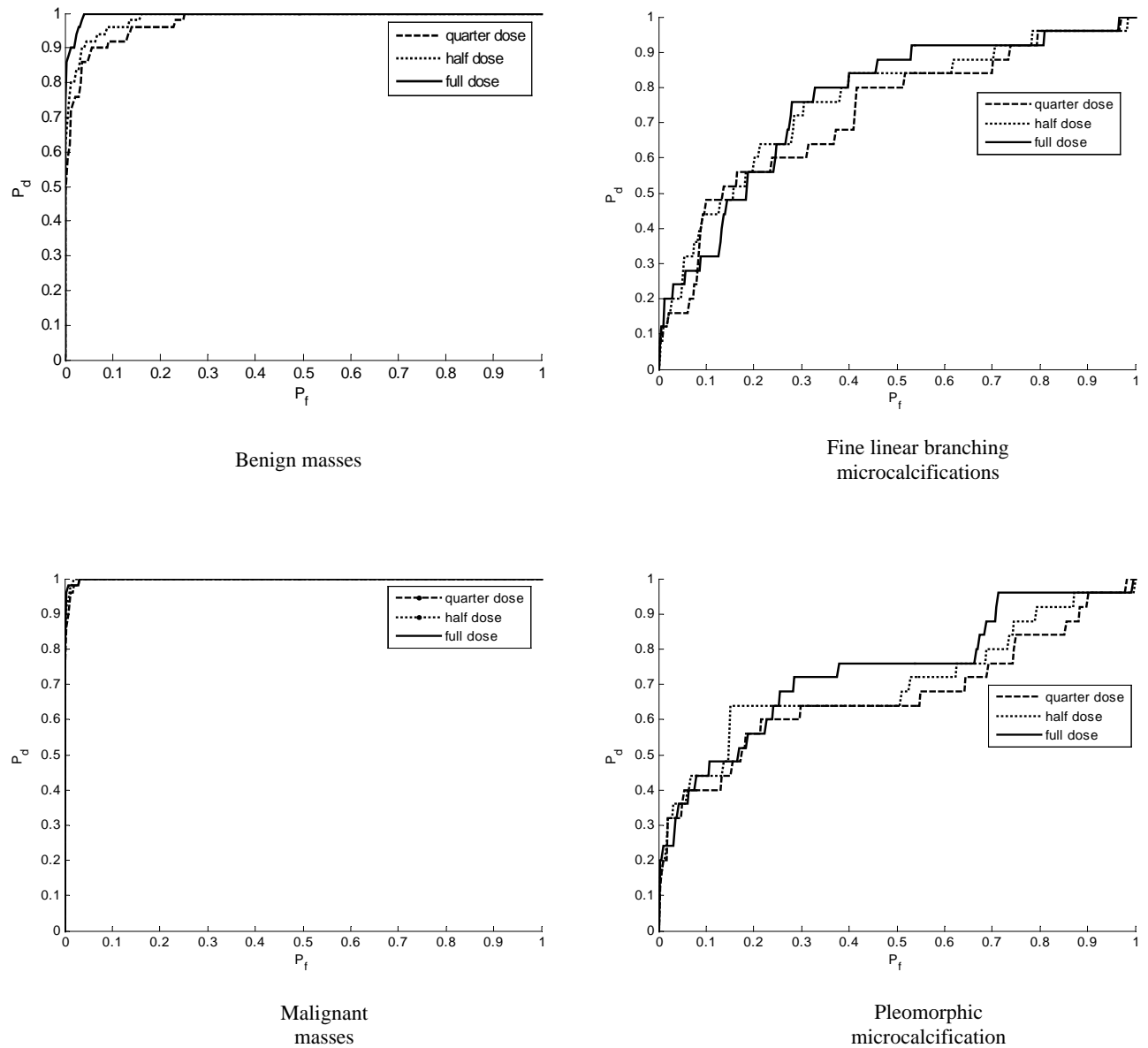


Fig. 5: ROC curves obtained with 56 Gabor Channelized Hotelling Observer

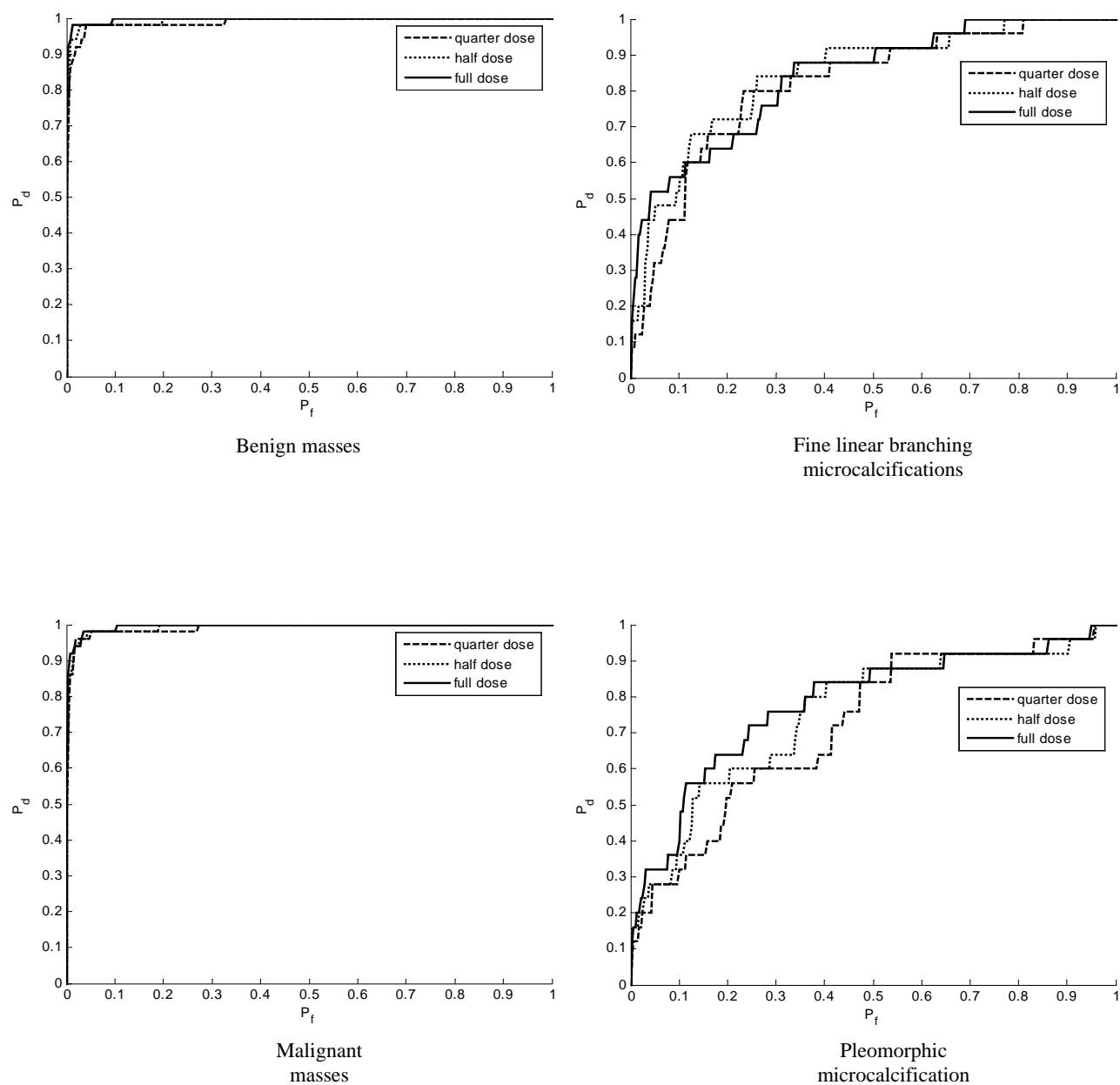


Fig. 6: ROC curves with Laguerre-Gauss Channelized Hotelling Observer

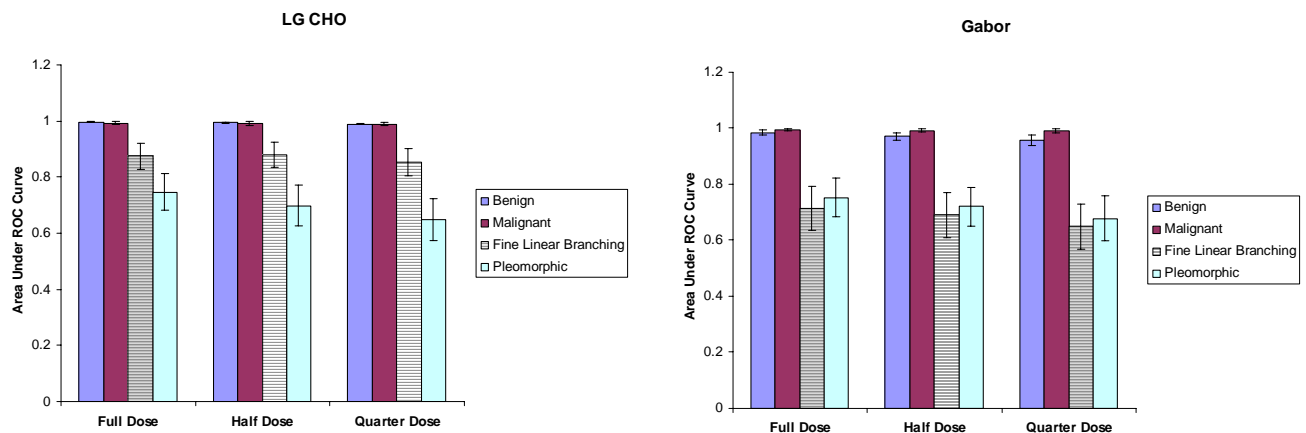


Fig. 7: Illustration of computed Area Under ROC Curves (AUC) and the associated standard errors. AUCs are used to quantify detection performance on mammograms acquired at three different dose levels. They were obtained from the two channelized Hotelling observers, namely Laguerre-Gauss and Gabor. Full-dose denotes the clinical dose level used in standard mammographic screening.

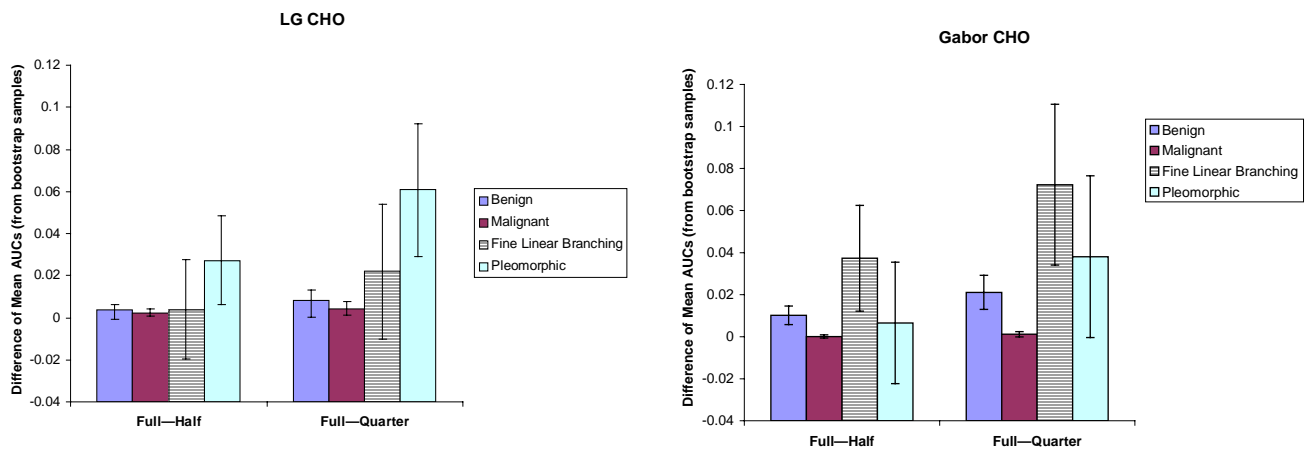


Fig. 8: Paired t-test analysis: Difference of mean AUCs obtained by bootstrap sampling of decision variables at different dose levels. The associated standard errors are also plotted.

DISCUSSION

In this study, we approximated a clinically relevant signal known statistically paradigm (23, 24) by using the recently introduced signal known exactly but variable (SKEV) framework. Under SKEV paradigm, a clinically relevant situation is approximated by changing the shape and size of signal from one image to another and the observer knows which signal will be present on the image before testing the image. In contrast, majority of previous studies done with observer models have used a signal-known-exactly (SKE) detection task where the same lesion whose shape and size are known *a priori* is embedded on set of different backgrounds which are either computer generated (25, 26) or real (16, 27). SKEV task has been used earlier on real anatomical backgrounds like angiograms (17) but as the final figure of merit only the detectability indices have been computed without a complete ROC analysis. In this work, we computed ROC curves as well as the Area under ROC Curve (AUC). The image backgrounds had real mammographic anatomical structures and hence were known only statistically.

Gabor CHO and LG CHO algorithmic observers suggested that a reduction in dose-level from the level currently used in mammographic screening procedures in clinics may not influence detection probability of most lesions on mammograms, although a statistical difference in performance of Gabor CHO was observed in the detection of benign lesions at different dose levels. There were no statistical differences in performance of the observer models as the dose was reduced to 50 % and or even 25%. However, there is an indication that the performance at 25% dose level may deteriorate more than when the dose is reduced by 50%. Mean difference in detectability increases when the dose is reduced from full to half level than when the dose is reduced from half to quarter level. These observations were also supported by NPWE and Hotelling observers. The SNR values decrease as dose is reduced from full dose to 50% and to 25% but the differences in the SNRs are within the standard error in measurement suggesting no strong evidence of any degradation in the performance with reduction of dose level. However, these observers have a clear drawback in that they assume statistical stationarity of the background. Reduction of dose may affect detection of microcalcifications more than masses, as indicated by higher mean difference in AUCs for microcalcifications than for masses. A previous study (28) also reported that dose reduction in digital mammography resulted in loss of microcalcification detectability due to an increase in noise. Furthermore, in contrast to the recent trends in increasing radiation dose in screen/film mammography (29), results in this study suggest that any further increase in dose-level than the clinical levels currently used, may not improve the detectability of mammographic lesions.

Despite the conclusions of this investigation, certain limitations should be acknowledged. One limitation of this research was the low number of images used for testing the performance of the mathematical observer models. At the same time the results do conform with the findings of another research group on phantoms (10) which concluded that a dose reduction by as much as 50% of the currently practiced clinical dose levels may not compromise clinical decisions. Furthermore, although the observer models have been shown to correlate well with human detection performance on real anatomical backgrounds, like mammograms, an exhaustive study has not yet been carried out to conclusively establish the correlation. It is therefore important that the significant potential of dose reduction found in this study should be implemented only after being confirmed clinically. Moreover, an important issue of the effect of reduced dose on discrimination between benign and malignant masses has not been addressed here.

CONCLUSIONS

In summary, patient dose in mammographic screening should be optimized for a balance between the radiation risk factor and the image quality required for detection task. This optimization should be based on clinical decision (that is the final outcome of the radiological process), rather than on absolute measures of image quality. All the algorithmic observer models used in this work show that reduction in dose-levels does affect detectability of masses and microcalcifications, although the differences are not statistically significant. This indicates that there is a potential for reduction of dose level in mammographic screening procedures without severely compromising the detectability of lesions. Dose reduction may, however, affect detection of microcalcifications more than the detection of masses. At the same time the results also suggest that any increase in dose level than the clinical levels currently used will not influence diagnostic performance. Furthermore, reduction of dose may have an effect on the

discrimination/classification of lesions. This and the present findings need additional confirmation by rigorous clinical trials and human observer studies before clinical implementation.

REFERENCES

1. NCRP, Mammography - a user's guide. In. Bethesda, MD: Report 85, National Council on Radiation Protection and Measurements (NCRP).
2. Kruger RL, Schueler BA. A survey of clinical factors and patient dose in mammography. *Med. Phys.* July 2001; 28:1449-1454.
3. Adler DD, Helvie MA. Mammographic biopsy recommendations. *Current Opinion in Radiology.* 1992; 4:123-129.
4. Bird RE, Wallace TW, Yankaskas BC. Analysis of cancers missed at screening mammography. *Radiology* 1992; 184:613-617.
5. NAS. (National Academy of Sciences) Health Risks from Exposure to Low Levels of Ionizing Radiation: BEIR VII-Phase 2. In. Washington, DC: National Academy Press, 2005.
6. Bochud FO, Verdun FR, Hessler C, Valley J-F. Detectability on Radiological Images: The Influence of anatomical noise. *Proceedings of SPIE Medical Imaging conference* April 1995; 2436:156-164.
7. Nishikawa RM, Vyborny CJ, Giger ML, Doi K. Analysis of false-positive microcalcification clusters identified by a mammographic computer-aided detection scheme. *Proceedings of SPIE Medical Imaging conference* 1994; 2167:773-777.
8. Law J, Faulkner K. Concerning the relationship between benefit and radiation risk, and cancer detected and induced, in breast screening programme. *British Journal of Radiology* 2002; 75:678-684.
9. Berns EA, Hendrick RE, Cutter GR. Performance comparison of full-field digital mammography to screen-film mammography in clinical practice. *Med. Phys.* 2002; 29:830-834.
10. Gennaro G, Katz L, Souchay H, Alberelli C, Maggio Cd. Are phantoms useful for predicting the potential of dose reduction in full-field digital mammography? *Phys. Med. Biol.* 2005; 50:1851-1870.
11. Robert S Saunders J, Samei E, Johnson J, Baker J. Effect of Display Resolution on the Detection of Mammographic Lesions. In: *Proc. of SPIE Medical Imaging Conference*, 2005; 243-250.
12. Saunders RS, Samei E. Characterization of breast masses for simulation purposes. In: *Proc. of SPIE conference on Medical Imaging*, 2004; 242-250.
13. Saunders RS, Samei E. A method for modifying the image quality parameters of digital radiographic images. *Med Phys* 2003;3006-3017.
14. Eckstein MP, Abbey CK, Bochud EO. The effect of image compression in model and human performance. In: *SPIE Proceedings of Image Perception and Performance*, 1999; 243-252.
15. Eckstein MP, Abbey CK, Whiting JS. Human vs. model observers in anatomic backgrounds. In: *SPIE Proceedings of Image Perception and Performance*, 1998; 15-26.
16. Burgess AE, Jacobson FL, Judy PF. Human observer detection experiments with mammograms and power-law noise. *Med. Physics* April 2001; 28:419-437.
17. Zhang Y, Pham B, Eckstein M. Task-based model/human observer evaluation of SPIHT wavelet compression with human visual system-based quantization. *Academic Radiology* March 2005; 12:324-336.
18. ICRU, Medical Imaging - The Assessment of Image Quality. In. Bethesda, MD: Report 54, International Commission on Radiation Units and Measurements (ICRU), 1996.
19. Samei E, Flynn M, Eyler WR. Detection of Subtle Lung Nodules: Relative Influence of Quantum and Anatomic Noise on Chest Radiographs. *Radiology* December 1999; 213:727-734.
20. Barrett HH, Abbey CK, Gallas B. Stabilized estimates of Hotelling observer detection performance in patient-structured noise. In: *Proc. of SPIE Medical Imaging Conference*, 1998; 27-43.
21. Burgess AE. Statistically defined backgrounds: performance of a modified nonprewhitening observer model. *J. Op. Soc. Am.* April 1994; 11:1237-1242.
22. A.B. Watson, Braddick OJ, Sleigh AC. Detection and recognition of simple spatial forms. In: *Physical and biological processing of images*. Berlin: Springer-Verlag, 1983.
23. Eckstein MP, Craig K. Abbey. Model observers for signal known statistically tasks. In: *SPIE Proceedings of Image Perception and Performance*, 2001; 91-102.

24. Eckstein MP, Zhang Y, Pham B. Optimization of model observer performance for signal known exactly but variable tasks leads to optimized performance in signal known statistically tasks. In:Proc. of SPIE Medical Imaging Conference, May 2003; 123-134.
25. Yang J, Cersaletti CD. Observer models and human visual detection performance with different targets. Proc. of SPIE Medical Imaging Conference 2004:319-329.
26. Burgess AE. Visual signal detection with two-component noise: low-pass spectrum effects. Journal of the Optical Society of America A 1999; 16:694-704.
27. Suryanarayanan S, Karellas A, Vedantham S, Ved H, D'Orsi CJ. Detection in compressed digital mammograms using numerical observers. Proc. of SPIE Medical Imaging Conference 2003; 5034:513-521.
28. Obenaus S, Hermann K, Schorn C, Fischer U, Grabbe E. Full-field digital mammography: dose-dependent detectability of simulated breast lesions. Fortschr Röntgenstr 2000; 172:1052-1056.
29. Pisano ED, Britt GG, Lin Y, Schell MJ, Burns CB, Brown ME. Factors Affecting Phantom Scores at Annual Mammography Facility Inspections by the U.S. Food and Drug Administration. Academic Radiology September 2001; 8:864-870.

A mathematical model approach towards combining information from multiple image projections of the same patient

Amarpreet S. Chawla¹, Ehsan Samei², and Craig Abbey³

Duke Advanced Imaging Laboratories

¹Departments of Radiology and of Biomedical Engineering, Duke University

²Departments of Radiology, Physics, Medical Physics and of Biomedical Engineering, Duke University

³Department of Biomedical Engineering, University of California, Davis

ABSTRACT

The purpose of this study was to, i) use a mathematical observer model to combine information obtained from multiple angular projections of the same breast to determine the overall detectability of a simulated lesion in a multi-projection breast imaging system and, ii) determine the optimum acquisition parameters of such a system. Multi-projection imaging is similar to tomosynthesis, except that the raw projection images are directly analyzed instead of reconstructing those images, thereby avoiding reconstruction artifacts. 25 angular projections of each breast from 82 human subjects in our tomosynthesis clinical trials were supplemented with projections from a simulated 3 mm 3D lesion. The lesion was assumed to be embedded in the compressed breast at a distance of 3 cm from the detector. The contrast of the lesion was determined taking into account the energy spectrum of the x-ray beam, properties of the digital detector, scatter fraction, and compressed breast thickness. A linear Hotelling observer with Laguerre-Gauss channels (LG CHO) was applied to each image. Detectability was analyzed in terms of ROC curves and the area under ROC curves (AUC). Three different methods were used to integrate ROCs from multiple (correlated) views to obtain one combined ROC as an overall metric of detectability. Specifically, 1) ROCs from different projections were simply averaged; 2) the test statistics from different projections were averaged; and 3) a Bayesian decision fusion rule was used. Finally, the number of angular projections, angular span and the acquisition dose level were optimized for highest AUC of the combined ROC as a parameter to maximize the performance of the system. It was found that the Bayesian decision fusion technique performs better than the other two techniques and likely offers the best approximation of the diagnostic process. Furthermore, if the total dose level is held constant at $1/25^{th}$ of the standard dual-view mammographic screening dose, the highest detectability performance is observed when considering only two projections spread along an angular span of 11.4° .

INTRODUCTION

Multiple-projection acquisition modalities such as Digital Breast Tomosynthesis (DBT), have been shown in the past to perform better than the standard projection procedures.¹ In recent implementations of DBT, a plurality of projection images are acquired along an arc pivoted about a point above the detector. These projection images are similar to standard mammograms, except that each of the images are acquired with lower dose level than in standard mammography. The images are then processed by image reconstruction algorithms to generate a multitude of in-plane image slices within the breast. Although this technique partially overcomes the limiting factor of overlapping anatomical structures, leading to increased conspicuity of lesions as compared to conventional mammograms, it is not without limitations. The number of slices generated by the reconstruction algorithm depends on the size of the breast. A radiologist may, therefore, need to review as many as 50-80 slices per breast to arrive at the final diagnostic decision as opposed to reviewing four views per mammographic exam. Moreover, lesion detection in tomosynthesis is dependent on the choice of image reconstruction technique, as well as the specifics of the implementation.² DBT is also prone to reconstruction artifacts. These factors may compromise the confidence or even accuracy of radiologist's decision.

An alternative to sorting through multiple slices is to review only the unreconstructed angular projections acquired in the process of tomosynthesis. Preliminary work in development of CAD algorithm, which fuses information from unreconstructed projection images, has demonstrated promising results.³ An important question, however, concerning

any multi-acquisitions technique such as this and also tomosynthesis, is what should be the acquisition parameters for optimum detection of breast lesions.

The key acquisition parameters are the total dose delivered to the patient, the number of angular acquisitions, and the total angular span of the acquisitions. Currently, there are no standard protocols for tomosynthesis acquisitions. Researchers have used 11 to 21 projections, with angular span varying from 30° to 60° , and the total dose to the patient ranging between 0.75-1 times the total two-view standard mammography dose-level.^{1, 3, 4} Recent work on tomosynthesis for detecting lung nodules has suggested an angular span of 3° to be optimal. However, other parameters such as dose and number of projections were not investigated.⁵

One way to investigate optimum operating acquisition parameters is to systematically change each of them w.r.t. each other and determine which one of the combinations yields the highest detectability of breast lesions. To assess the detectability of lesions, a clinical study involving human observers may be conducted. However, such an approach is costly and complex. Another approach is to use mathematical observers that model the diagnostic process. Such observers have been used in the past to predict the performance of human observer in clinically realistic tasks.⁶⁻¹⁰

An observer model was designed to assess the Receiver Operating Characteristic (ROC) curve associated with the detectability of a lesion at each angular projection. The ROCs from different projections were then combined using three techniques.

The goal of this study was two-fold: i) to compare three different techniques using a mathematical observer model to combine information obtained from multiple angular projections of the same breast to determine the overall detection performance of a multi-projection imaging system in detectability of a simulated mass, and ii) to determine the optimum dose level, the number of angular projections and the total angular range.

MATERIALS AND METHODS

A. Image Database

The study employed a database of images of the left and right breasts of 82 subjects. Images were acquired about the CC or MLO orientation from 25 different but fixed angular positions by a prototype clinical multi-projection system, Siemens' Mammomat Novation^{DR} (Fig. 1). The system used a clinical selenium-based, flat-panel, digital mammography detector of array size 2816×3584 and with a pixel pitch of $85 \mu\text{m}$. The system used a tungsten target, a $50 \mu\text{m}$ rhodium filter, a source to image distance (SID) of 65.32 cm, and had an iso-centric geometric pivoting of the x-ray tube about a point located 6 cm above the detector. The projection angles of the 25 images were varied between $\pm 25^\circ$ angular range about the central orientation (CC or MLO) in 2° steps. The tube voltage ranged between 28 and 30 kVp. The total dose delivered to the patient from 25 angular acquisitions was equivalent to that delivered in a standard two-view mammographic screening procedure, with each angular projection at a dose level, D_θ , equal to $1/25^{\text{th}}$ of the total dose. All images were judged to be free from suspicious lesions.

Using the database, 492 ROIs (2 breasts \times 82 patients \times 3 ROIs/projection) of size 512×512 each were extracted. The displacement of the ROIs on the detector across the different angular projections was taken into account so that the ROIs from the same patient represented the same section of the breast. From these, 264 were used for training the observer model, while the remaining 228 ROIs were used for testing.



Fig. 1: The prototype multi-projection breast imaging instrument.

B. 3D Lesion Simulation

The ROIs generated above were inserted with a simulated mammographic lesion, 3 mm in diameter. The lesion was simulated in 3D. To do so, first a target 2D projection profile based on a previously published model of lung nodules,^{11, 12} also applied to mammographic applications.¹³ Starting from this profile, the surface of the central slice of the lesion was reconstructed using inverse radon transform, assuming that the lesion is isotropic and the different angular projections along the plane of the central slice would yield the same profile across the central slice. The central slice was then rotated about its diameter to complete the simulation of a 3D lesion.

Next, projections of this 3D lesion from the 25 angular positions of the tube onto the center of different ROIs were computed taking into account the position of the ROI on the detector and assuming that the lesion was embedded in the compressed breast (2-8 cm in thickness) at a distance of 3 cm from the detector. The x and y coordinates of the projected lesion on the image plane were determined as,

$$\begin{aligned} x_i &= \frac{x * (D + L \cos \phi) - z * L \sin \phi}{D + L \cos \phi - z} \\ y_i &= \frac{y * (D + L \cos \phi)}{D + L \cos \phi - z} \end{aligned} \quad (1)$$

where (x, y, z) are the positional coordinates of any point on the lesion, (x_i, y_i) are the corresponding coordinates in the image plane, and L and D are the distances of the pivotal point from the source and the detector, respectively. These equations were derived based on the trajectory of the acquisition system and are similar to those derived by others.^{14,15} Fig. 2 shows projection of the 3-D lesion on the detector from three different tube angular orientations of $+21.89^\circ$, 0° , and -22.94° relative to the CC orientation.

The lesions were embedded onto the different ROIs to generate 492 signal-present ROIs for each angular projection. The ratio of the contrast of the lesion to its diameter (set to 3 mm) was determined from published contrast/lesion thickness ratios based on the acquisition kVp, target/filteration combination, compressed breast thickness, and detector type.¹¹ This ratio was further modified to take scattering into account. Towards that end, scatter to primary ratio were computed based on 80/20% glandular tissue/fat breast composition. The lesions were then added to the ROI in the log space such that the contrast of the lesion over the background was independent of the breast composition. Fig. 3 shows images of ROIs with the simulated lesion embedded at the center.

C. Noise Simulation

Following extraction of ROIs, a noise modification routine was used to add radiographic noise to each of the ROIs to create images with a noise appearance similar to that caused by further reduction in radiation dose from D_θ . Noise equivalent of a particular dose level was determined using a novel algorithm, which has been reported earlier in detail.¹⁶ The algorithm accounted for the quantum noise variance, the detector transfer properties and its noise characteristics, and the impact of varying attenuation due to breast structures. By changing the noise magnitude, 24 dose-reduction levels, corresponding to $D_\theta/2$ to $D_\theta/25$, were simulated. These with the original clinically acquired images resulted in images with 25 contiguously decreasing dose levels. Fig. 3 shows ROIs with different dose levels. While Fig. 3(a) shows the original clinically acquired image, Fig. 3(b), and (c) show the same ROI with added simulated noise corresponding to reduced dose level of $D_\theta/2$, and $D_\theta/25$, respectively.

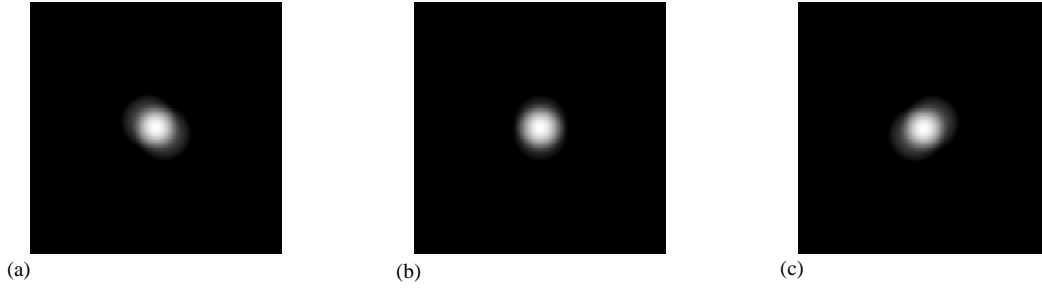


Fig. 2: Example images of projections of 3-D model of a 3 mm simulated lesion assumed to be 3 cm above the detector. These lesions were embedded on tomographic projections to emulate the lesion-present mammographic background. (a), (b), and (c) show the projections with the tube orientation at $+21.9^\circ$, 0° , and -22.9° , respectively, relative to the CC orientation.

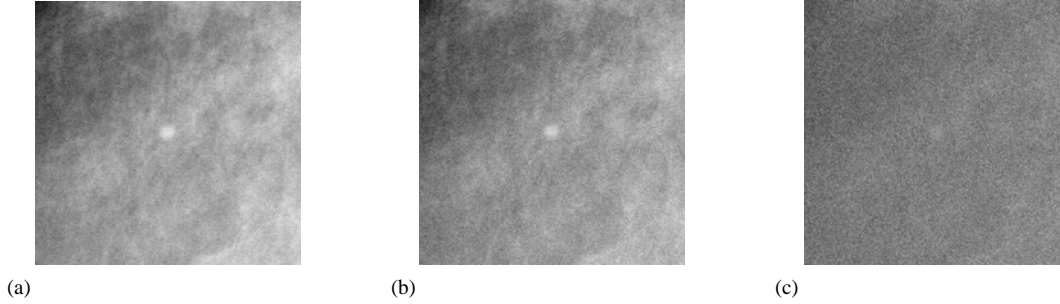


Fig. 3: Example images of ROIs with simulated lesion embedded at the center. The ROIs were extracted from full-field tomographic projections, following which, projections of 3D model of a 3 mm lesion were embedded at the center of each of these ROIs. (a) shows ROI of a clinically acquired projection with dose level, D_θ , equal to $1/25^{\text{th}}$ that of standard mammographic screening. (b), and (c) show the same ROI with noise corresponding to $1/2$, and $1/25^{\text{th}}$ fraction of D_θ .

D. Mathematical Observer Model

Mathematical observer models have been used to predict human observer performance in clinically relevant visual tasks such as the detection of lesions in a complex background structure. It has been shown earlier that linear observers models like Hotelling observers are good predictors of human visual performance under various tasks over real anatomic backgrounds¹⁷⁻²⁰. A computationally simpler version of Hotelling observer, namely the Laguerre-Gauss Channelized Hotelling Observer (LG CHO) was used in this study. LG CHO uses linear features that are a product of *Laguerre* polynomials and *Gaussians* functions for reducing the dimensionality of the Hotelling observer, thus making the implementation simpler. The functions use a distance scale related to the signal radius. This value which defines the variance of the *Gaussian*, is iteratively adjusted to maximize the area under the ROC curves. A value of 10 was found to maximize AUC in the present study. A total of 10-channels were used (generally 6 channels are sufficient for characterizing isotropic signals²¹). As shown in Fig. 2, the signals (simulated lesions) used in our study were isotropic within certain degrees of approximation. The covariance matrix of the LG CHO was trained with signal-absent ROIs. While testing using the LG CHO, signal in each of the ROIs was analyzed with the signal-known exactly (SKE) methodology, assuming that the lesion embedded on different ROIs within the same angular projection have approximately the same shape. ROCs for each of the 25 angular projections were obtained using a methodology reported earlier.⁶

E. ROC Fusion

25 ROCs obtained from the 25 angular projections are indicative of the performance of an observer as it analyzes each of those projections independently, i.e. unmindful of the correlation between the projections. The task of the present study was to fuse the 25 ROCs into one final index of performance. Towards that end, three methods were used. For the first method, the 25 ROCs were simply averaged along the true positive fractions to yield the combined ROC associated with the detection of lesion in all the projections. In the second method, the signal-present and signal-absent test statistics from different projections were averaged to determine the final test statistics. These values were then used to determine the combined ROC.

For the third ROC fusion method, a modification of a recently published Bayesian decision fusion algorithm was used.²² In this case, first ROC for each angular projection in the training dataset was determined. The training dataset comprised of 429 ROIs for each angular projection. Next, for each of the 69 ROIs in the testing dataset, signal-present decision variable was calculated by determining the response of the image embedded with i^{th} lesion to i^{th} lesion template and the corresponding signal-absent response by determining the response of the image itself (without the lesion embedded) to the i^{th} lesion template. Binary observer decision, β_i , to the i^{th} image was computed as

$$\begin{aligned}\beta_i &= \text{step}(\lambda_1^i - \lambda_0^i) \\ &= \begin{cases} 1 & \text{if } \lambda_1^i \geq \lambda_0^i \\ 0 & \text{if } \lambda_1^i < \lambda_0^i, \end{cases}\end{aligned}\quad (2)$$

i.e., the binary decision for an i^{th} image was 1 if the signal-present decision variable, λ_1^i , exceeded signal-absent decision variable, λ_0^i , but 0 otherwise. From the above equations it is clear that the threshold for correct observer outcome of an i^{th} image is λ_0^i . The corresponding values of probability of true positive, p_d , and of false positives, p_f , were determined from the ROCs of the 25 angular projections in the training dataset. Assuming that the binary decisions were statistically independent, the PDFs of the fused decision variables for signal-present and null hypothesis were then obtained as

$$\begin{aligned}P(\lambda_{fusion} | H_1) &= \prod_{\theta=1}^{25} (p_d^\theta)^{\beta_i} (1 - p_d^\theta)^{1-\beta_i} \\ P(\lambda_{fusion} | H_0) &= \prod_{\theta=1}^{25} (p_f^\theta)^{\beta_i} (1 - p_f^\theta)^{1-\beta_i},\end{aligned}\quad (3)$$

where, θ is an index for angular projection. Having found the signal-present and signal-absent decision variables, the probability density functions of each were computed and ROC determined.

F. Evaluating optimum acquisition parameters

The ROC fusion methodologies were applied to evaluate the effect of changing original acquisition parameters at each of the 25 dose levels. The two parameters evaluated were the angular range of projections and the number of angular projections within each angular range. Furthermore, two dose conditions were evaluated:

- (a) the *iso-image dose condition* in which all the angular projections considered for final figure of merit have the same dose levels resulting in increasing total delivered dose with each additional angular projection, e.g., evaluating performance from fusing decisions from N acquisitions, each at a dose level of D_0 , resulting in a total delivered dose of ND_0 , and
- (b) the *iso-study dose condition* in which incorporating additional angular acquisition in the study does not result in increased total dose delivered to the patient, i.e. only acquisitions with dose levels of D_0/N are used for analyzing the final performance index from N acquisitions, resulting in a fixed total delivered dose of D_0 . Optimum acquisition parameter was determined as the combination of dose level, number of angular projections and the angular range which yield the maximum area under the combined ROC.

RESULTS

ROC curves and the corresponding AUCs obtained from the three techniques are shown in Fig. 4. While AUC obtained from a single CC projection was 0.652, AUC obtained from an average of ROCs obtained from 25 projections was 0.642. Simple averaging of test statistics yielded an AUC of 0.815. An AUC of 0.946 was obtained from the Bayesian decision fusion technique.

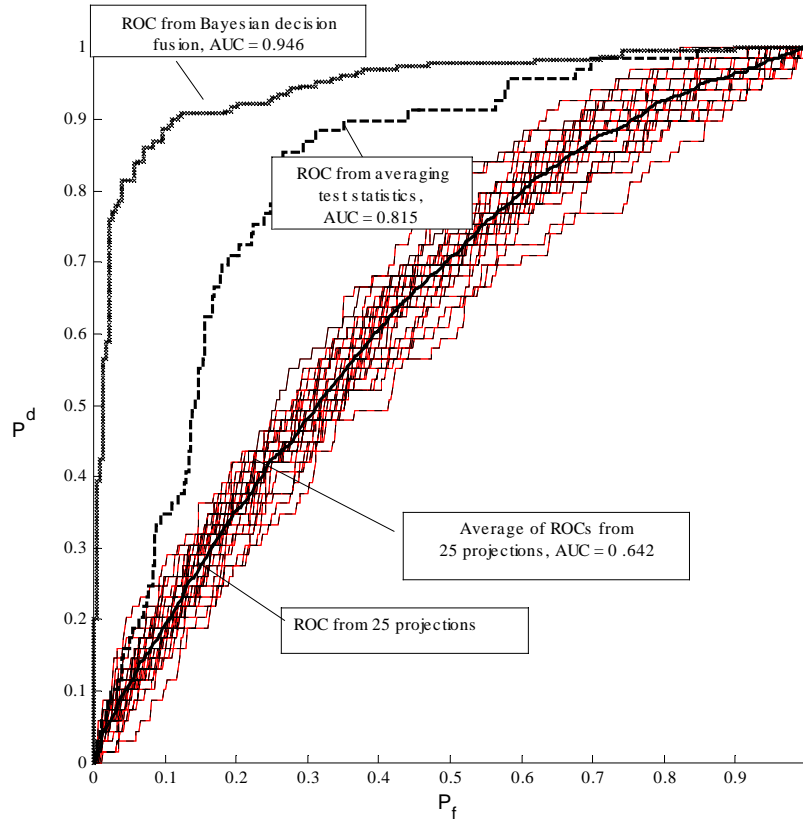


Fig. 4: ROCs of 25 projections and the average of those with the final AUC = 0.6417. Also shown are the ROCs obtained from the three other fusion techniques. The angular span of the projections was 44.8° .

Fig. 5 shows variation of AUC under iso-image dose conditions for different number of angular projections spanning a total angular arc in the 3.6 - 44.8° range using the Bayesian decision fusion technique. The dose level of each acquisition is equal to $1/25^{th}$ of standard mammographic screening dose-level leading to increased dose level with increasing number of angular projections considered. At each angular range, the AUC increases with the increase in number of angular

projections, however, the change in AUC in each case is minimal after 10 projections. Noteworthy, is the fact that an angular span of 11.4° yields the highest AUC when fusing only two projections.

Fig. 6 shows variation of AUC under iso-study dose conditions using the Bayesian decision fusion technique. In this case, the total dose level is linearly divided amongst the different projections and hence the total dose delivered does not increase with an increase in the number of projections considered for decision fusion. For all angular spans, the AUC first increases and then decreases as the number of projections are increased. The iso-image and iso-study dose conditions for two angular spans – 44.8° and 11.4° , are collated in Fig. 7. Both figures show that under iso-study dose conditions, the highest AUC is obtained by combining information from just two projections with an angular span of 11.4° .

Fig. 8 shows the variation of AUC obtained by different fusion techniques under iso-study dose conditions. The total angular span was held constant at 44.8°

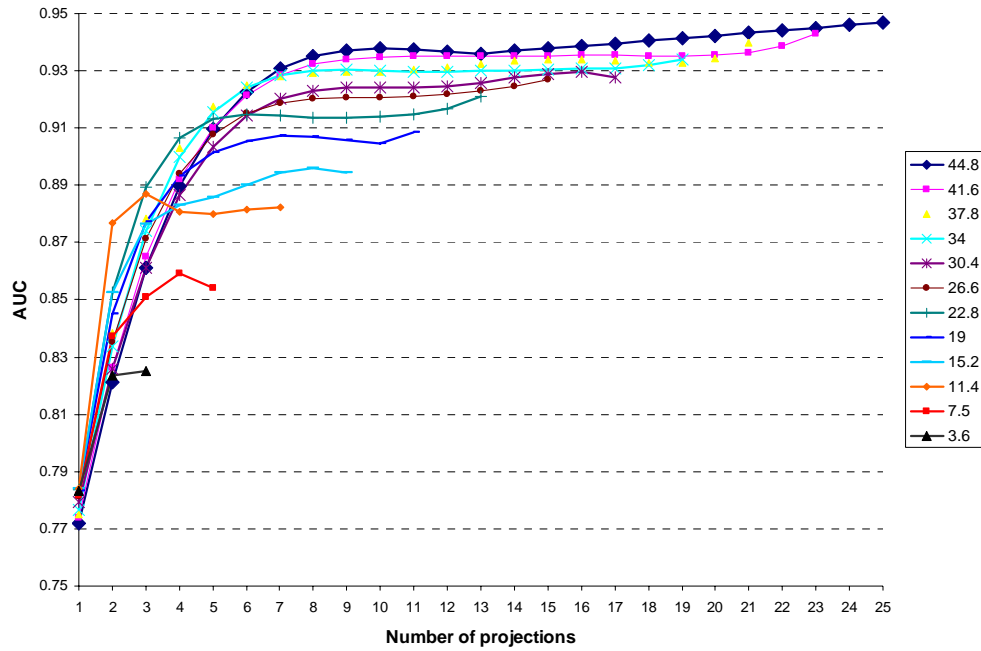


Fig. 5: Variation of AUC under iso-image dose conditions for different number of angular projections spanning a total angular arc in the 3.6 - 44.8° range using the Bayesian decision fusion technique. The dose level of each acquisition is equal to $1/25^{th}$ of standard mammographic screening dose-level leading to increased dose level with increasing number of angular projections considered to reach a maximum of conventional dual-view screening dose at 25 projections.

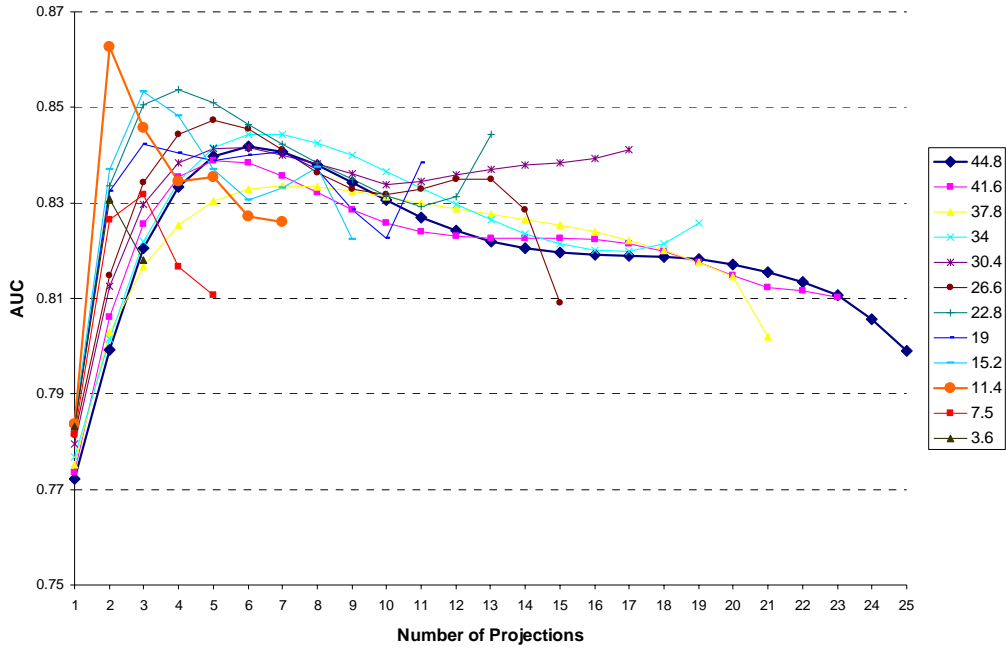


Fig. 6: Variation of AUC under iso-study dose conditions using the Bayesian decision fusion technique. The total dose level, equal to $1/25^{th}$ of standard dual-view mammographic screening dose level, is linearly divided amongst the different projections and hence the total dose delivered remains constant at this dose level.

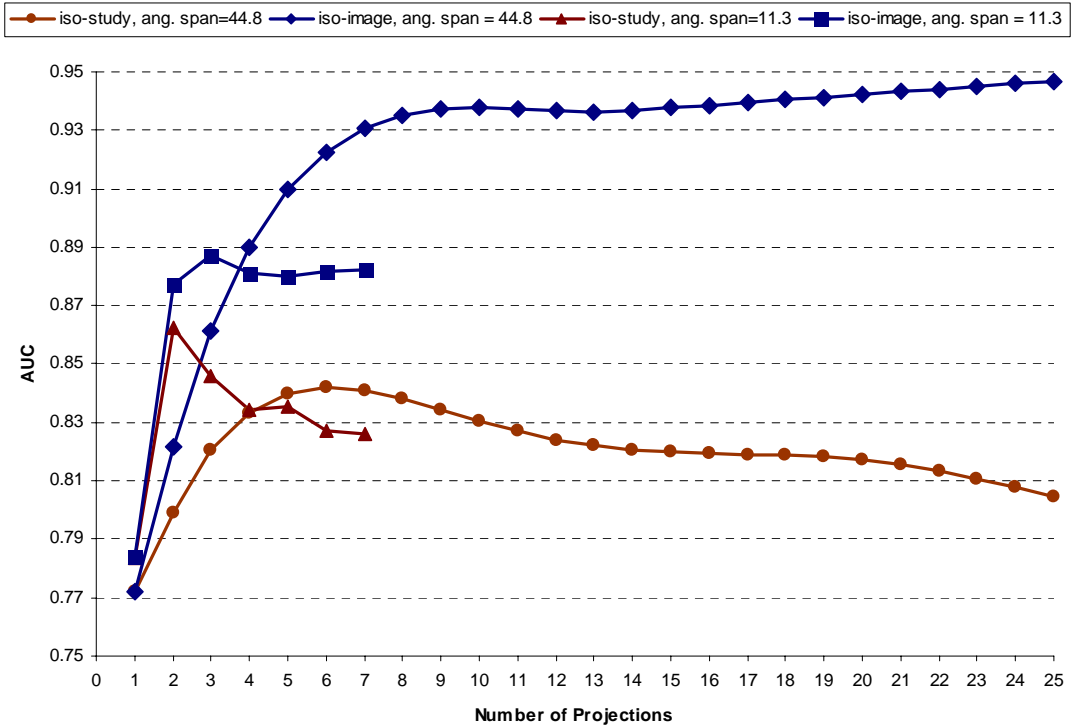


Fig. 7: Comparison of iso-image dose (at $1/25$ of standard dual-view mammographic screening dose-level, D_θ) and iso-study dose conditions (at D_θ for the whole study) for two angular spans – 44.8° and 11.4° , using Bayesian decision fusion technique.

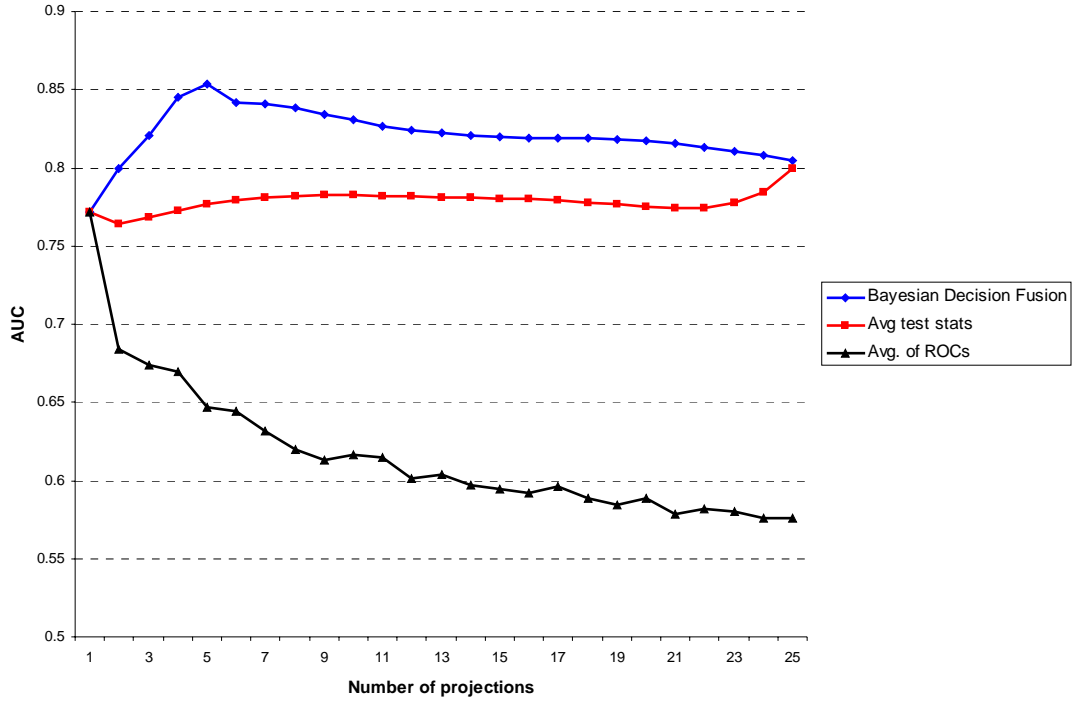


Fig. 8: Variation of AUC obtained by different fusion techniques under iso-study dose conditions. The total angular span was held constant at 44.8° .

DISCUSSION

The methodology used in this study quantifies the effect of changing acquisition parameters on the image quality in terms of detectability of a simulated mass. To the best of our knowledge, such a study has not been undertaken before. Each of the three acquisition parameters investigated in this study has a clinical implication. While having multiple images of the same breast potentially increases the cues for the detection of pathology, it also adds the dose delivered to the patient (iso-image dose condition). Alternatively, total dose may be equally distributed among all the projections as the number of projections is increased such that the total dose is held constant (iso-study dose condition). In this case, however, as the number of projections is increases, the dose level of each projection decreases, severely compromising the image quality due to the reduction of the signal-to-noise-ratio in each projection. This reduction in image quality may, however, be offset by added information provided to the observer by increased number of projections. These potentially conflicting factors may thus introduce an inflection point in the over all detectability of a mass, as indeed shown in Figs. 6 and 8. In this study, we show that it is possible to separate the question of dose delivered to the patient from the number of projections needed for an optimal detection task using an iso-study dose condition. Our study showed that at a given total dose level, the best performance can be obtained using only two projections.

We found that the detectability is dependent on the total angular span of the projections. The performance is better at lower angular spans. This may be because at larger source angles, the x-ray beam has larger path resulting in higher attenuation of the beam. In this study, we used three techniques to fuse information from these multiple images of the same breast to arrive at one final figure of merit indicating overall detectability of a simulated mass. Out of the three fusion techniques, simple averaging of ROCs or of test statistics do not emulate a clinical decision processes. Using these techniques, under iso-study dose conditions, the AUCs either decrease or remain relatively constant with increase in the number of projections (Fig. 8).

The third technique, Bayesian decision fusion, may be understood in the following way: given an image from angular projection, θ , assuming that the decision for signal present is 1, the probability of correct detection is p_d^θ . However, if the decision is 0, the probability that the signal is still present is the probability of false negative and hence $(1 - p_d^\theta)$.

Thus the resultant probability of signal present in the image is $p_d^\theta \cdot (1 - p_d^\theta)$. Assuming statistical independence of decisions among angular projections gives the PDFs of the fused decision variables of eq. (3). It may be noted that statistical independence of only binary decisions of the 25 classifiers were assumed, however, correlation information between contiguous images has not been taken into account. It may be noted that statistical independence of only binary decisions of the 25 classifiers were assumed, however, correlation information between contiguous images has not been taken into account. However, the Bayesian decision technique closely emulates the decision process used by human observers in arriving at the final decision.

One of the limitations of this study was the fact that we could not evaluate performance at arbitrary number of angular projections for each angular span. This is because we were limited by the sampling of the original clinical images which was uniform within each angular span. This is evident in Figs. 5, 6, and 7 where AUC values were plotted for fewer angular projections as the angular span decreases. Furthermore, because we could only simulate a reduction of exposure levels by adding corresponding noise onto the images, only one iso-study dose condition of total dose of D_θ could be investigated (D_θ corresponding to $1/25$ of standard two-view mammographic screening dose). Furthermore, although the observer models have been shown to correlate well with human detection performance on real anatomical backgrounds, like mammograms, an exhaustive study has not yet been carried out to conclusively establish the correlation. Hence it is important that the results of the study be clinically validated. For our future work, we plan to extend our study to imaging cadaver specimens.

Reducing the number of acquisition images has certain advantages. While it may provide superior image data for a signal detection, it can make the process more comfortable for the patient, reduces possible motion artifacts, and reduces the total acquisition time. However, the advantages of a reduced number of projections need to be confirmed with the dose level for the examination kept at the same level as that of standard screening. That assessment should await further studies.

CONCLUSIONS

Mathematical observer models can be used to predict the performance of a multi-projection acquisition system. Detectability of lesion was found to be dependent on the number of projections used, the total angular span of those projections and their acquisition dose level. An optimization technique to quantify the effects of changing acquisition parameters was established. It was found that if the total dose level is held constant at $1/25^{th}$ of the standard dual-view mammographic screening dose, the highest detectability performance is observed when considering only two projections spread along an angular arc of span 11.4° . Future work will confirm this optimization at higher dose levels. The methodology presented here for optimizing acquisition parameter are generic in nature and, therefore, can be easily adopted for optimizing the acquisition parameters for other breast imaging methods, such as Digital Breast Tomosynthesis, where the final figure of merit is contingent on decisions made on a plurality of image slices.

ACKNOWLEDGMENTS

We would like to thank Jonathan Jesneck for helpful discussions on the Bayesian decision fusion methodology. We would also like to thank Rob Saunders and Joseph Lo for their valuable assistance. This work was supported in part by the Breast Cancer Research Program - Pre-Doctoral Traineeship grant no. W81XWH-06-1-0449, NIH grant no. R01-CA109074 and a grant from Cancer Research Prevention Foundation.

REFERENCES

- ¹ X. Gong, S. J. Glick, B. Liu, A. A. Vedula and S. Thacker, "A computer simulation study comparing lesion detection accuracy with digital mammography, breast tomosynthesis, and cone-beam CT breast imaging," *Med. Phys.* **33**, 1041-1052 (2006).
- ² L. Zhou, J. Oldan, P. Fisher and G. Gindi, "Low-contrast lesion detection in tomosynthetic breast imaging using a realistic breast phantom," *Proc. SPIE* **6142**, 61425AI-A61412 (2006).
- ³ I. Reiser, R. M. Nishikawa, M. L. Giger, et al., "Computerized mass detection for digital breast tomosynthesis directly from the projection images," *Med. Phys.* **33**, 482-491 (2006).
- ⁴ Y. Zhang, H.-P. Chan, B. Sahiner, et al., "A comparative study of limited-angle cone-beam reconstruction methods for breast tomosynthesis," *Med. Phys.* **33**, 3781 (2006).
- ⁵ A. R. Pineda, S. Yoon, D. S. Paik and R. Fahrig, "Optimization of a tomosynthesis system for the detection of lung nodules," *Med. Phys.* **33**, 1372 (2006).
- ⁶ A. S. Chawla, R. Saunders, C. Abbey, D. Delong and E. Samei, "Analyzing the effect of dose reduction on the detection of mammographic lesions using mathematical observer models," *Proceedings of SPIE* **6146**, 61460I-61461 - 61460I-61412 (2006).
- ⁷ A. E. Burgess, F. L. Jacobson and P. F. Judy, "Human observer detection experiments with mammograms and power-law noise," *Med. Phys.* **28**, 419-437 (April 2001).
- ⁸ S. Suryanarayanan, A. Karellas, S. Vedantham, H. Ved and C. J. D'Orsi, "Detection in compressed digital mammograms using numerical observers," *Proc. SPIE* **5034**, 513-521 (2003).
- ⁹ J. Yang and C. D. Cerosaletti, "Observer models and human visual detection performance with different targets," *Proc. SPIE* **5372**, 319-329 (2004).
- ¹⁰ A. E. Burgess, "Visual signal detection with two-component noise: low-pass spectrum effects.," *J. Op. Soc. Am. A* **16**, 694-704 (1999).
- ¹¹ R. S. Saunders, E. Samei and C. Hoeschen, "Impact of resolution and noise characteristics of digital radiographic detectors on the detectability of lung nodules," *Med. Phys.* **31**, 1603-1613 (2004).
- ¹² E. Samei, M. Flynn and W. Eyler, "Simulation of subtle lung nodules in projection chest radiography," *Radiology* **202**, 117-224 (1997).
- ¹³ A. E. Burgess, F. L. Jacobson and P. F. Judy, "Human observer detection experiments with mammograms and power-law noise," *Med. Phys.* **28**, (2001).
- ¹⁴ L. Niklason, B. Christian, L. Niklason, et al., "Digital tomosynthesis in breast imaging," *Radiology* **205**, 399-406 (1997).
- ¹⁵ J. T. Dobbins and D. J. Godfrey, "Digital x-ray tomosynthesis: current state of the art and clinical potential," *Phys. Med. Biol.* **48**, R65-R106 (7 October 2003).
- ¹⁶ R. S. Saunders and E. Samei, "A method for modifying the image quality parameters of digital radiographic images," *Med. Phys.* **30**, 3006-3017 (2003).
- ¹⁷ M. P. Eckstein, C. K. Abbey and E. O. Bochud, "The effect of image compression in model and human performance.," *SPIE Proceedings of Image Perception and Performance* **3663**, 243-252 (1999).
- ¹⁸ M. P. Eckstein, C. K. Abbey and J. S. Whiting, "Human vs. model observers in anatomic backgrounds," *SPIE Proceedings of Image Perception and Performance* **3340**, 15-26 (1998).
- ¹⁹ A. E. Burgess, F. L. Jacobson and P. F. Judy, "Human observer detection experiments with mammograms and power-law noise," *Med. Physics* **28**, 419-437 (April 2001).
- ²⁰ Y. Zhang, B. Pham and M. Eckstein, "Task-based model/human observer evaluation of SPIHT wavelet compression with human visual system-based quantization.," *Academic Radiology* **12**, 324-336 (March 2005).
- ²¹ H. H. Barrett, C. K. Abbey and B. Gallas, "Stabilized estimates of Hotelling observer detection performance in patient-structured noise," *Proc. of SPIE Medical Imaging Conference* **3340**, 27-43 (1998).
- ²² J. L. Jesneck, L. W. Nolte, J. A. Baker, C. E. Floyd and J. Y. Lo, "Optimized approach to decision fusion of heterogeneous data for breast cancer diagnosis," *Med. Phys.* **33**, (2006).